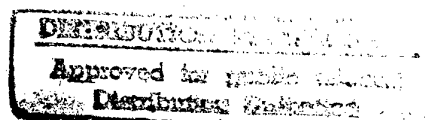


DETECTION OF PLASMA CLUSTERS WITH THIN MAGNETIC FILMS

Technical Feasibility Study

*Fourth quarterly progress report
(Final report)*

Special Project No. SPC-93-4022



19961113 145

ALL INFORMATION CONTAINED HEREIN IS UNCLASSIFIED

Andrzej Maziewski

Laboratory
of Magnetism

Institute of Physics
Warsaw University Branch

41 Lipowa Street

15-424 Białystok, POLAND

Tel.: (48-85)22491, (48-85)22492 ;

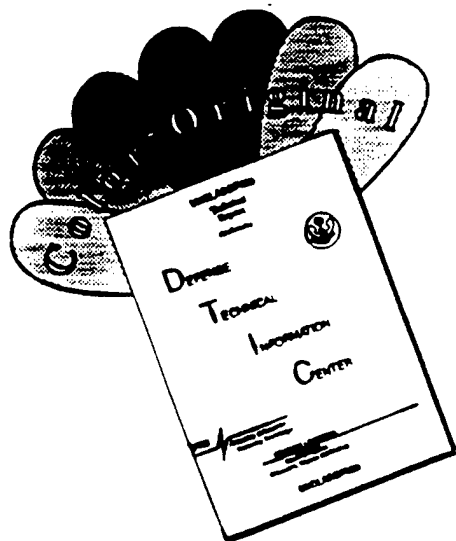
Fax: (48-85)20272

Tlx.: 853350 fuw

E-mail: MAGNET@CKSR.AC.BIALYSTOK.PL



DISCLAIMER NOTICE



THIS DOCUMENT IS BEST QUALITY AVAILABLE. THE COPY FURNISHED TO DTIC CONTAINED A SIGNIFICANT NUMBER OF COLOR PAGES WHICH DO NOT REPRODUCE LEGIBLY ON BLACK AND WHITE MICROFICHE.

REPORT DOCUMENTATION PAGE			Form Approved OMB No. 0704-0188	
Public reporting burden for this collection of information is estimated to average 1 hour per response, including the time for reviewing instructions, searching existing data sources, gathering and maintaining the data needed, and completing and reviewing the collection of information. Send comments regarding this burden estimate or any other aspect of this collection of information, including suggestions for reducing this burden to Washington Headquarters Services, Directorate for Information Operations and Reports, 1215 Jefferson Davis Highway, Suite 1204, Arlington, VA 22202-4302, and to the Office of Management and Budget, Paperwork Reduction Project (0704-0188), Washington, DC 20503.				
1. AGENCY USE ONLY (Leave blank)	2. REPORT DATE 1994	3. REPORT TYPE AND DATES COVERED Final Report		
4. TITLE AND SUBTITLE Detection of Plasma Clusters within Thin Magnetic Films			5. FUNDING NUMBERS SPC-93-4022	
6. AUTHOR(S) Andrzej Maziewski				
7. PERFORMING ORGANIZATION NAME(S) AND ADDRESS(ES) Institute of Physics Warsaw University Branch 41 Lipowa Street 15-424 Bialystok, Poland			8. PERFORMING ORGANIZATION REPORT NUMBER SPC-93-4022	
9. SPONSORING/MONITORING AGENCY NAME(S) AND ADDRESS(ES) EOARD PSC 802 BOX 14 FPO AE 09499-0200			10. SPONSORING/MONITORING AGENCY REPORT NUMBER SPC-93-4022	
11. SUPPLEMENTARY NOTES				
12a. DISTRIBUTION/AVAILABILITY STATEMENT Unlimited			12b. DISTRIBUTION CODE	
13. ABSTRACT (Maximum 200 words) Our experiments have established novel method of dense plasma domains detection and visualisation. It was shown that dense plasma domains with enhanced reactivity, PDER, (trapping ions of MeV/nucleon energies) when interacting with a thin film of magnetic garnet, TF-MG, changes drastically its domain structure properties. Magnetic treatment of the films, ensuring the best contrast of the PDER image, is specified and PDER image is shown in the mode of domain dimensions. Different kinds of Faraday's rotation modes are also possible. Comparative analysis of PDER, detected with spots of accelerator-implanted D ⁺ ions of different energies and total doses, supported with numerical simulation of the process, allows to define figure of merit physical parameters of the object under study. It was found that visualised PDER has linear dimension of <1 mm, accompanied by 1 cm long "tail" of lower density. Detection of D ⁺ ions is limited to the energy range of 1MeV < E < 2MeV by thickness of front filter and TF-MG thickness. These characteristics are similar to those define by nuclear methods for PDERs observed far from the pinch.				
14. SUBJECT TERMS			15. NUMBER OF PAGES 80	
			16. PRICE CODE	
17. SECURITY CLASSIFICATION OF REPORT UNCLASSIFIED	18. SECURITY CLASSIFICATION OF THIS PAGE UNCLASSIFIED	19. SECURITY CLASSIFICATION OF ABSTRACT UNCLASSIFIED	20. LIMITATION OF ABSTRACT UL	

ABSTRACT

Our experiments have established novel method of dense plasma domains detection and visualisation. It was shown that dense plasma domains with enhanced nuclear reactivity, **PDER** (trapping ions of MeV/nucleon energies) when interacting with a thin film of magnetic garnet, **TF-MG**, changes drastically its domain structure properties. Magnetic treatment of the films, ensuring the best contrast of the PDER image, is specified and PDER image is shown in the mode of domain dimensions. Different kinds of Faraday's rotation modes are also possible. Comparative analysis of PDER, detected with spots of accelerator-implanted D^+ ions of different energies and total doses, supported with numerical simulation of the process, allows to define figure of merit physical parameters of the object under study. It was found that visualised PDER has linear dimension of <1 mm, accompanied by 1 cm long 'tail' of lower density. Detection of D^+ ions is limited to the energy range of $1\text{MeV} < E < 2\text{MeV}$ by thickness of front filter and TF-MG thickness. These characteristics are similar to those define by nuclear methods for PDERs observed far from the pinch.

1. INTRODUCTION

Plasma focus (PF) discharges [1] are well-known sources of plasma domains with fast ions and enhanced plasma fusion, PDER. In one discharge, the PF machine (stored energy of the powering capacitor bank $W=7\text{kJ}$) filled with deuterium accelerates, traps and ejects 10^{12} D^+ ions of $E>0.5$ MeV. The majority of these, fast-ions come from a few PDERs [2,3]. The form factor of ion energy spectrum (normalized to unity) can be expressed in the following form:

$$\frac{dN}{dE} \cong \frac{(m-1) E^{-m}}{E_0^{(1-m)}}$$

up to $E=10$ MeV [4]. $m \cong 2.5$ and E_0 is the minimal energy of detected ions. PDERs have linear dimensions of $d \sim 0.5$ mm [5,6], composed of plasma of density of $n > 10^{22}/\text{cm}^3$ [2,3,7,8] and have temperature of $kT > 1$ keV [8,9]. PDERs nature is barely known, some hypothesis links fast ions production to the explosive decay of the magnetic structures of organized plasma filaments [10,11]. In present situation, when one can identify position, explosion time of and measure PDERs energy spectra the urgent demand is to have efficient means for PDER imaging. The goal of this project is to find out if the thin film of magnetic garnets, TF-MG [13], can be a useful detector. As a presentation method of final results we choose the journal publication style, while the details of particular experiments and their analysis can be found in the appendixes.

2. EXPERIMENTAL

2.1 Samples

The TF-MG material is considered as the most promising candidate for PDERs detector/recorder. In particular, the 3-in diameter $(\text{BiTm})_3(\text{FeGa})_5\text{O}_{12}$ garnet films has been grown by liquid phase epitaxy method on [111] oriented gadolinium gallium garnet substrate [14]. Epitaxial garnet films were used for model investigation of magnetic and magneto-optical properties for many years [15, 16-18], so the previous experience can be used in the interpretation of PDER - TF-MF interactions. As result of the applied technology, material of the following parameters was obtained: thickness ca. $7 \mu\text{m}$ (equivalent to the range of D^+ ions of $E \cong 1$ MeV),

stripe domain period $p \approx 50 \text{ } \mu\text{m}$, $4\pi M < 100 \text{ Gs}$; magnetic anisotropy field $< 2000 \text{ Gs}$. One and the same TF-MG sample was divided into several targets and some of them were exposed to D^+ ion implantation, other to the PF discharges. The difference is, that implanted fragments are covered with $0.05 \mu\text{m}$ aluminum while in the PDER registration the TF-MG surface is protected with $12.5 \mu\text{m}$ mylar foil (equivalent to the range of D^+ ions of $E \approx 950 \text{ keV}$) to shield it from large fragments of discharge filaments carrying large currents of low energy ions.

2.2 Samples Calibration

Calibration of TF-MF was done using the high density implantation of D^+ ions of well established energy and dose. To have a quantitative calibration, the implantation was done on a fragment of the same sample as was exposed to the PDERs interactions. For details of implantation experiments and best methods of the implanted area visualisation see Ref. [19-21], Appendixes 2-4. Implantations were done by the VdG electrostatic accelerator at Soltan Institute for Nuclear Studies, Warsaw. TF-MG areas exposed to the D^+ beam were of quasi-rectangular shape with 1 mm^2 surface obtained by the proper openings in the tantalium stopers. A special care was taken to assure that the beam of deuterons impinging a target is fully ionized (better than 0.99). Implantation was done for nine different conditions covering expected PDER characteristics i.e. $E = 0.5 \text{ MeV}$, 1.0 MeV and 1.6 MeV (energy resolution $\Delta E/E < 0.05$) and doses for each D^+ energy of $N[1/\text{mm}^2] = 10^{14}$, 10^{15} and 3×10^{15} (with uncertainty of 5%). Implanted part of the TF-MG was covered by $0.05 \mu\text{m}$ aluminum layer for keeping the sample in neutral electric state during implantation.

A Monte-Carlo simulation of the density distribution of the irradiation defect, caused by D^+ ions in the unlimited thickness $(\text{BiTm})_3(\text{FeGa})_5\text{O}_{12}$ garnet, are shown in Fig.1. The figure was prepared for energies $E = 0.5$, 1 and 1.6 MeV . These energies roughly correspond to D^+ ion energy of 1.5 , 2 and 2.6 MeV , in conditions of TF-MG exposure during PF experiment. Because the major defect density (and D^+ deposition) occurs at the sample depth close to the particle range, the effects induced by 1.6 MeV deuterons are less effective, see Figs.8-10.

2.3. Experimental Set-up for TF-MG Exposure to PDER Generated in the Plasma Focus Machine.

The PDERs recording was done at Stevens Institute of Technology, Hoboken, NJ. The experimental set-up is shown in the Fig.2. PF- machine was fired at the stored energy of the capacitor bank $W=7\text{kJ}$ and the discharge chamber is filled to 4.5 Torr deuterium (0.999). These conditions are typical for so called 'neutron mode of operation'. The compressed plasma, additionally to deuterium has Cu impurities picked-up from the electrodes. Impurities do not exceed of 10^{-5} of the compressed plasma content. The TF-MG targets (exposed one at the time) were protected with the $12.5\mu\text{m}$ mylar foil meant to protect surface from damage by fragments of plasma carrying large currents of low energy ions. The same protective foil was used during the traditional recording with CR-39 [5,6] track detector. The mylar foil completely stops ions of energies $E<950\text{keV}$. It is well established that number of PDERs emitted during one discharge, of this particular PF machine, very rarely exceeds five units per discharge [3] so exposure of samples and number of required discharges was governed by the laws of probability. For that reason samples after exposure were preliminary scanned and experiment continued till the recording of the PDER fingerprint occurred. The task was simplified as from the previous experience with CR-39 target it is known what type of fingerprint to expect. Fortunately we recorded PDER signature without needing to double (or more) expose the same TF-MG samples to PF discharge.

2.4 Instrumentation for Reading of the PDER Images

The D^+ ion implanted spots (from accelerator and/or PDERs) detection was based on two independent methods related to change in: (a) the dimension (and pattern) of domains, see Fig.5a and (b) the Faraday's rotation in TF-MG dependent on the ion implantation parameters, see Fig.3. Magneto-optical scanning of domain structure of exposed garnet was realized using optical polarizing microscope set-up, supported by digital image processing system (see Fig.4) (described in Ref.[19], Appendix 2), examples are shown in Ref.[20,21], Appendixes 3,4. As most effective diagnostics of PDERs, we found the specially developed digital image processing methods such as 'light polarization modulation method' [22,23]. This was used in our previous reports. This method supported by novel spatial filtering and thresholding techniques [23,24,25] could be used to obtain high quality images, even for low contrast objects. For PDERs, inducing higher changes of magnetic anisotropy, it will

be possible to analyse the spatial distribution of these changes by combining discussed above digital image processing method and method of magneto-optical magnetometry [26-28].

3. PDER VISUALIZATION AND ITS PHYSICAL CHARACTERISTICS

3.1 PDER Visualization

The images of the PDER recorded by TF-MG are shown in Fig.5a. For comparison, in Fig.5b PDER recorded with CR-39 track detector are shown. However, one should be aware that the image obtained with CR-39 comes from different shot and at different location of the detector. In both cases the PDERs are recorded due to impact on recording surface (covered with $12.5\mu\text{m}$ mylor foil). Parameters of the PF discharge for which PDER was recorded, are as follows: $W=5\text{kJ}$, $p=4.5\text{ Torr (D}_2\text{)}$, neutron yield $Y_n=7\times 10^8$ (typical for this machine). One can see that the recorded PDER images have a comet-like form, a 'head' and a 'tail' can be distinguished. Additionally, the visualisation of the PDER recorded on TF-MG was done by a several other discussed below techniques and are shown in Fig.6.

3.2 Domain Structure Investigation

For comparison of the properties of the TF-MG domain structure inside and outside of PDER, it is convenient to introduce a domain wall length L parameter, measured per unit area of the sample surface. Looking at Fig.5a,6, it is easy to notice, that in the 'head' area the L parameter depends on the magnetic treatment of the sample. Domain structures were obtained applying magnetic field perpendicular to the film plane H_{\perp} quasi-static or $H_{\perp\text{ac}}$ alternating with different amplitude. The L parameter is either significantly smaller (almost saturated 'head' area of the sample - a large white domain area in Fig.5a) or larger (Fig.6) in comparison with the one measured outside of the PDER. The first case was obtained after the sample saturation (about 200 Oe field amplitude was used) while decreasing H_{\perp} to zero. The second one - after sample demagnetization by $H_{\perp\text{ac}}$ alternating magnetic field with amplitude decreasing from about 200 Oe to zero. In the 'tail' area, the L parameter continuously decreases along the following route: starting from the end of the 'head'

through the 'tail' to an undefected place. The dependences of the L parameter on the magnetic field H_{\perp} are shown in Fig.7a,b for the two different procedures of magnetic treatment. Details of the L parameter study are described in Appendix 1.1. This study shows real possibility of PDER distinguishing on the base of analysis of the L parameter.

Magnified, small areas of the comet 'head' and 'tail', as well as implanted and unaffected sample, are shown in Fig.8. One can find similarity of domain size in the 'head' area with the implanted with $E=1\text{MeV}$ and $N=10^{14}$ area. However, domain shape in the 'head' region is sharper. This is explained by higher coercivity in this region. A discussion of domain structures in all implanted samples is given in Appendix 1.1.

3.3 Magnetometer Measurements

Faraday rotation $\varphi(H_{\perp}, H_{\parallel})$ dependencies were measured as a function of magnetic field applied perpedicularly H_{\perp} and parallel H_{\parallel} to the plane of the sample. The φ parameter is proportional to the magnetization component, perpendicular to the plane of the sample. $\varphi(H_{\perp}, H_{\parallel})$ dependencies, measured for PDER and implanted samples, are shown in Fig.9 and Fig.10. From the $\varphi(H_{\perp})$ data presented in these figures one could deduce the lack of paramagnetic sublayer in the PDER. On the contrary, the paramagnetic sublayer do exists in almost all of the implanted samples. $\varphi(H_{\parallel})$ dependeces allowed to determine the magnetic anisotropy and its changes along the depth of the sample. Solid line in Fig.10 stand for calculated data, which were obtained by fit to the experiment, using a simple three-sublayer model of the sample - details of the model and calculed anisotropy parameters can be found in Appendix 1.2. From the anisotropy data analysis one can deduce: (a) the changes of magnetic anisotropy in the 'head' area, (b) localization of these changes in somewhat deeper, close to substrate, part of the magnetic layer. After this analysis one could roughly estimate the energy range of D^+ ions which produced the 'head'. The energy was higher than 1.5MeV (we took into consideration also the energy lost in the mylor) and lower than 2.5MeV.

3.4 Monte-Carlo Simulation

Numerical simulations of deuteron transport in a garnet-like target were executed using Monte Carlo methods for three different energies E of impact ions. Irradiation defect density distributions $G(z)$ along the distance z (calculated from the sample surface), were collected for 100000 events of impacting ions. Results of the simulation are shown in Fig.1 in a form of $G(z)$ dependencies. The changes of magnetic properties depend strongly on the defects concentration. A limit defects concentration, which is sufficient to cause the transformation to the paramagnetic state, could be estimated on the basis of both $G(z)$ dependencies and paramagnetic sublayer thickness taken from an experiment. In our case, it was most convenient to determine the thickness h_D for the implantation with $E=1.0$ MeV and $N=10^{14}$ (using the hysteresis loops - Fig.9). A diagram $p_{hc}(E,N)$ of constant value of paramagnetic sublayer thickness was constructed in the (E,N) coordinates for $7\mu\text{m}$ -total-thickness-sample using both the limit density defects value estimated in above described manner and the $G(z,E)$ distributions - see Fig.11.

This $p_{hc}(E,N)$ diagram could be helpful in estimating the irradiation dose, which acted in the garnet sample during the impact of the plasma cluster. As was mentioned above, the hysteresis loops, measured both in the 'head' and 'tail' areas (see Fig.9), show lack of paramagnetic sublayer. Thus, the upper limit of dose of plasma cluster are thought to be in the range of 10^{13} .

Due to the dependence of paramagnetic susceptibility of the paramagnetic sublayer on density of impact ion beam, this susceptibility may additionally be used for analyzing the irradiation density of high ion density plasma cluster.

3.5 Discussion

At this stage of our investigation, we bring the possibility of precise determination of the plasma cluster parameters into question. Undoubtedly, the changes of both domain dimension and magnetic anisotropy in the 'head' area, are noticeable. But it is now difficult to describe these effects using a simple model, regarding implantation energy and dose, because the implantation processes are very complex and they produce heterogeneous changes of magnetic properties along the thickness of the sample. This heterogeneity is not visible directly in our measurement, where magneto-optical properties averaged over total thickness, are detected.

This unfavorable state could be changed for the better after the execution of additional, more subtle investigations. The list of further investigation should include:

1. Magnetometer measurements in higher range of magnetic fields.
2. Implantation of D^+ with a broader range of energy and dose (implantations, which had been realized before, caused much stronger changes in garnet magnetic properties in comparison with the changes, introduced by the plasma cluster, PDER).
3. Measurements of the magnetic properties after gradual removing of the surface layer of the sample by etching.
4. More accurate numeric simulation of deuteron transport in garnet (simulation, which had been done before, was probably oversimplified: the target, used in calculation, had the density similar to garnet, but the composition was restricted up to four different elements and the target had to be amorphous).

4. CONCLUSIONS

The most important findings of presented study are the following:

1. Thin garnet films are suitable for the new method of the plasma cluster detection.
2. Magnetic treatment of the garnet films, ensuring the best contrast of the exposed areas, is specified and easy achievable experimentally.
3. Energy (in the range from 1.5 MeV to 2.5MeV) and dose ($10^{12} < N < 10^{13}$) of plasma cluster radiation is very roughly estimated on the basis of both magnetic measurements of the D^+ ion implanted spots (from accelerator and PDERs) and Monte-Carlo simulation of trapping of D^+ ion in garnet target. More accurate informations of the plasma cluster parameters could be obtained after realization the extended investigations

Now when principles of new method of PDERs imaging are proven, the new tool for exotic plasma study is established. The method can be applied as it is with simultaneous refinement of scanning and automatization of process.

REFERENCES:

- [1] J.W.Mather, in: Methods of Experimental Phys. (Academic, New York,1971) Vol 9, p.197
- [2] J.S.Brzosko and V.Nardi, Phys. Lett. A155 (1991) 162
- [3] J.S.Brzosko, V.Nardi, J.R.Brzosko, and D.Goldstein, Phys. Lett. A192 (1994) 250
- [4] V.Nardi, A.Bortolotti, J.S.Brzosko, M.Esper, C.M.Luo, F.Pedrielli, C.Powell and D.Zeng, IEEE Trans. PS-16 (1988) 368
- [5] V.Nardi, A.Bortolotti, J.S.Brzosko in: Plasma Physics and Controlled Fusion Research (1988) IAEA-CN-50 Vol.2 (IAEA, Vienna, 1989) 743
- [6] M.Sadowski et al., Phys. Lett. A113 (1985) 25
- [7] G.R.Neil and R.S.Post, Plasma Phys. 14 (1988) 425
- [8] I.Volobuev et al., Siv.J.Plasma Phys. 14 (1988) 401, 622
- [9] J.S.Brzosko, B.V.Robouch and J.Klobukowska Nucl./Fusion Techn. 4 (1983) 263
- [10] W.H.Bostick, L.Grunberger, V.Nardi and W.Prior, in: Proc. 5th Symp. on Thermophysical Properties (Am.Soc.Mech.Eng., New York, 1970) 495
- [11] V.Nardi, Phys. Rev. Lett.25 (1970) 718
- [12] A.Bortolotti, J.S.Brzosko, F.Mezzetti, V.Nardi, C.Powell and D.Zeng, in: Controlled Fusion and Plasma Heating (Ed. European Phys. Soc., 1988) ECA 12B (1988) 613
- [13] A.H.Eschenfelder, Magnetic bubble technology, Springer Series in Solid State Sciences 14, Berlin (1981)
- [14] P.Görnert, F.Voigt, Current Topics in Materials Science, ed. E.Kaldis (North-Holland, Amsterdam, 1984) 11.
- [15] P.Hansen et al., 'Iron Garnets', Landoldt-Bornstein, New Series, Vol 12a (Springer, Berlin, 1977)
- [16] Z.A. Kazei et al., 'Garnets' Landoldt-Bornstein New Series, Vol 27, subvolume e (Springer-Verlag, Berlin, 1991)
- [17] A.Maziewski, J.Magn.Magn.Mat. 88 (1990) 325
- [18] A.Maziewski, Ferrites Proc. ICF 6 Tokyo (1992) 782
- [19] A.Maziewski, First quarterly progress report on the Special Project No. SPC-93-4022
- [20] A.Maziewski, Second quarterly progress report on the Special Project No. SPC-93-4022
- [21] A.Maziewski, Third quarterly progress report on the Special Project No. SPC-93-4022
- [22] E.Kubajewska, A.Maziewski, A.Stankiewicz, Thin Solid Films 175 (1989) 299
- [23] A.Maziewski, K.Mroczek, A.Stankiewicz, M.Tekielak, M.Kisielewski ICMO'91 Kharkov, Fiz.Niz.Temp. 18 Suppl. S1 (1992)

- [24] E.Kubajewska, A.Maziewski, A.Stankiewicz, Acta Phys. Polonica A77 4 (1990) 159
- [25] M.Kisielewski, A.Maziewski, J.M.Desvignes, paper presented in ICM'94 Warsaw, accepted for publication in J.Magn.Magn.Mat (1994)
- [26] A.Maziewski, A.Stankiewicz, M.Tekielak, V.V.Volkov ICMO'91 Kharkov, Fiz.Niz.Temp. 18 Suppl. S1 (1992)
- [27] V.Grolier, J.Ferre, A.Maziewski, E.Stefanowicz, D.Renard J.Appl.Phys. 73 10 (1993) 5939
- [28] M.Marysko, A.Maziewski, A.Stankiewicz, M.tekielak, V.V.Volkov, Physica B 190 (1993) 190
- [29] A.Maziewski, E.Stefanowicz, V.Tarasenko, J.Ferre, V.Grolier, D.Renard, paper presented in ICM'94 Warsaw, accepted for publication in J.Magn.Magn.Mat (1994)

APPENDIX 1

A.1.1. L parameter study

Dependencies of the domain wall length L as a function of the magnetic field H_{\perp} (applied perpendicularly to the plane of the sample) were studied, see Fig.7 (in the final report). This L parameter was measured in three selected areas : (i) 'head', (ii) 'tail' and (iii) the outside of the 'comet' region. L depends on the sample magnetic treatment. Two different procedures of this treatment are discussed.

First procedure: (i) H_{\perp} magnetic field was applied with a higher amplitude than the one $H_{\perp s}$ necessary to the sample saturation (the $H_{\perp s}$ field amplitude decreases on the route starting from the 'head' to an undefected place); (ii) $L(H_{\perp})$ was measured changing magnetic field from $+H_{\perp s}$ to $-H_{\perp s}$ or from $-H_{\perp s}$ to $H_{\perp s}$, arrows in Fig.7 show this history. The difference $|H_{\perp n} - H_{\perp s}|$ between $H_{\perp n}$ domain nucleation field and $H_{\perp s}$ domain saturation field is much higher in the 'head' than in an undefected place. After decreasing H_{\perp} to zero the 'head' area remains saturated. Thus this area is easy distinguishable, see Fig.5a. From the Fig.7 one can also find a difference in the L parameter measured in the 'tail' and an undefected place. This effect can also be used for 'tail' localization. Generally the plasma cluster trace could be detected looking at domain structure at the field $H_{\perp} \neq 0$.

Second procedure. The sample had been demagnetized by $H_{\perp ac}$ alternating magnetic field with the amplitude decreasing from 200 Oe down to 0 Oe. The $L(H_{\perp}=0)$ parameter was measured and marked in Fig.7. A particular strong dependence of the $L(H_{\perp}=0)$ parameter in the 'head' on magnetic treatment is visible in this figure. There is strong difference between the $L(H_{\perp}=0)$ parameter measured in these three areas, see Fig.7 and Fig.8. Thus, this second procedure could be also used to uncover the plasma cluster trace, see Fig.6.

Similar domain structure images, obtained for implanted samples, are shown in Fig.8. In five cases the domain structure have been observed, but in the case of implantation energy 1.0 MeV and 1.6 MeV and dose 10^{15} and 3×10^{15} it has not been observed, because of the paramagnetic state of these samples - see hysteresis loops drawn in Fig.9. Implantation induced both decrease and increase of L parameter which is visible in Fig.8. This result could be roughly explained in the following terms : (i) Lower doses of defects induce a decrease of magnetic anisotropy. It causes lowering of domain wall energy σ_w , resulting in the decrease of material lenght parameter $l = \sigma_w / 4\pi M^2$ (where M is magnetization). The final result is an increase of domain wall length, see Fig.8 (the case of ions implantation with 1 MeV,

$N=10^{14}$); (ii) Increase of defects concentration induces increase of local sample coercivity - resulting in the increase of domain structure sensitivity on these defects, see Fig.8 for the case of ions implantation with $E=0.5\text{MeV}$, $N=10^{14}$, 10^{15} , 3×10^{15} . Similar effect is observed in material (e.g. ultrathin magnetic films) where local coercive force is higher than other forces - e.g. magnetostatic one [29]. Parameter $L(H_L=0)$ was measured after sample demagnetization, using second procedure (ac field), see Table 1. The data in Table 1 shows the possibility of distinguishing the defected areas on the base of analyzing of the L parameter. Differences between L values, obtained in different areas, are much greater than the statistical deviation of each value.

Table 1. Parameter L measured at $H_L=0$ after executing the ac-field sample demagnetization procedure.

Area	L_1 [mm]	L_2 [mm]	L_3 [mm]	L_4 [mm]	L_5 [mm]	L_{aver}^* [mm]	σ^* [mm]
undefected	5.93	5.73	5.62	5.14	5.71	5.63	0.29
'head'	23.03	22.88	22.10	21.19	18.72	21.58	1.76
'tail 1'***	11.39	10.93	11.11	10.93	11.45	11.16	0.25
'tail 2'***	9.62	10.02	9.94	10.18	9.49	9.85	0.29
'tail 3'***	7.81	7.87	7.86	8.07	7.76	7.87	0.12
$E=0.5\text{MeV}$, $N=10^{14}$	0.70	0.70	0.70	1.31	0.70	0.82	0.27
$E=0.5\text{MeV}$, $N=10^{15}$	1.15	1.04	1.06	1.29	0.88	1.08	0.15
$E=0.5\text{MeV}$, $N=3 \times 10^{15}$	1.61	0.59	0.84	0.81	1.60	1.09	0.48
$E=1.0\text{MeV}$, $N=10^{14}$	28.91	31.54	31.43	31.56	28.98	30.48	1.40
$E=1.0\text{MeV}$, $N=10^{15}$	0.0	0.0	0.0	0.0	0.0	0.0	0.0
$E=1.0\text{MeV}$, $N=3 \times 10^{15}$	0.0	0.0	0.0	0.0	0.0	0.0	0.0
$E=1.6\text{MeV}$, $N=10^{14}$	7.61	7.97	7.91	7.73	8.13	7.87	0.20
$E=1.6\text{MeV}$, $N=10^{15}$	0.0	0.0	0.0	0.0	0.0	0.0	0.0
$E=1.6\text{MeV}$, $N=3 \times 10^{15}$	0.0	0.0	0.0	0.0	0.0	0.0	0.0

*Both L_{aver} average value and σ standard deviation of L , was calculated on the base of five measurement of L (L_i , $i=1, \dots, 5$).

***Tail 1', 'tail 2' and 'tail 3' mean different parts of the 'tail' area, they were chosen at a distance of ca. 1mm, 2mm and 3mm relative to the center of 'head' area, respectively.

A.1.2. Magnetic Anisotropy Study

As it was mentioned above, the existence of the paramagnetic sublayer in almost all of the implanted samples, could be deduced on the base of the $\varphi(H_{\perp})$ curves shown in Fig.9. The thickness $h_p(E,N)$ of the paramagnetic sublayer could be approximated by:

$$h_p(E,N) = 1 - \frac{\varphi_{\max}(E,N)}{\varphi_{\max}(\text{nonimpl})}$$

where $\varphi_{\max}(E,N)$ and $\varphi_{\max}(\text{nonimpl})$ are maximum values of Faraday rotation φ in the implanted (with energy E and dose N) areas and in non-implanted area, respectively (the φ_{\max} value could be either directly measured in large H_{\perp} field or could be obtained by approximation). In the case of all implanted samples - except the one implanted with $E=1.6\text{MeV}$ and $N=10^{14}$ - the following relation is valid:

$$\varphi_{\max}(E,N) < \varphi_{\max}(\text{nonimpl})$$

what justifies our deduction. Moreover, in the case of four implantation, characterized by $E=1.0\text{ MeV}$, 1.6 MeV and $N=10^{15}$, 3×10^{15} , the $\varphi(H_{\perp})$ curves indicate the paramagnetic state in the whole volume of magnetic layer.

Let us compare the $\varphi(H_{\perp})$ curves obtained for areas: non-implanted and implanted with the lowest energy (0.5 MeV) at increasing doses. One can conclude, that this implantation have caused changes in limited volume of the sample. In the case of the lowest dose ($N=10^{14}$) a change of type of magnetic anisotropy took place (from uniaxial to in-plane anisotropy). In the case of two higher doses, the whole implanted sublayer became paramagnetic and a smaller paramagnetic susceptibility could be noticed.

Measurements of $\varphi(H_{\parallel})$ dependencies allowed to determine the magnetic anisotropy and its changes along the distance from the sample surface. Solid line in Fig.10 marks calculated data, which were obtained as a result of fitting to the experimental data with the following assumption: the sample was set to be three-sublayer; the first and the second magnetic sublayers had the thickness h_a and h_b , and the uniaxial anisotropy field H_{u_a} and H_{u_b} , respectively. The third one was paramagnetic with the thickness h_p and the paramagnetic susceptibility χ . Results of the fitting are summarized in Table 2.

The analysis of Table 2 shows the following features of our sample: (a) 'undefected' sample is heterogeneous and consists of two sublayer characterized by different both anisotropy fields and thicknesses ($h_a=0.3$, $h_b=0.7$), (b) on the base of destruction of the $h_b=0.7$ sublayer, accomplished by the shortest-in-range implantation with $E=0.5\text{MeV}$, one could conclude, that this sublayer is localized near the top surface of the sample (surface between film and air), (c) in the 'head' area,

the significant change of anisotropy field occurs in the $h_a=0.3$ sublayer, i.e. in deeper sublayer (surface between film and the substrate).

Table 2. The H_{u_a} , H_{u_b} uniaxial anisotropy field, h_a , h_b magnetic sublayer thicknesses, h_p paramagnetic sublayer thickness and χ paramagnetic susceptibility obtained by simultaneous fitting to the $\phi(H_{||})$ and $\phi(H_{\perp})$ curves, using three-sublayer model of the sample.

Area	h_a^*	H_{u_a} [kOe]	h_b	H_{u_b} [kOe]	h_p	χ [deg/kOe]
undefected	$0.34 \pm 0.02^{**}$	2.44 ± 0.1	0.66 ± 0.02	0.42 ± 0.04	0.0	-
'head'	0.30 ± 0.02	1.34 ± 0.2	0.70 ± 0.02	0.35 ± 0.06	0.0	-
'tail'	0.30 ± 0.02	2.42 ± 0.2	0.70 ± 0.02	0.48 ± 0.05	0.0	-
$E=0.5\text{MeV}$, $N=10^{14}$	0.33 ± 0.05	0.04 ± 0.2	0.35 ± 0.05	-0.31 ± 0.1	0.32	***
$E=0.5\text{MeV}$, $N=10^{15}$	0.28 ± 0.01	3.33 ± 0.4	0.03 ± 0.01	-0.52 ± 0.2	0.69	***
$E=0.5\text{MeV}$, $N=3 \times 10^{15}$	0.24 ± 0.01	3.56 ± 1.4	0.00 ± 0.01	-	0.76	***
$E=1.0\text{MeV}$, $N=10^{14}$	0.17 ± 0.03	2.40 ± 2.0	0.45 ± 0.03	0.14 ± 0.2	0.38	***
$E=1.0\text{MeV}$, $N=10^{15}$	0.0	-	0.0	-	1.0	0.31 ± 0.03
$E=1.0\text{MeV}$, $N=3 \times 10^{15}$	0.0	-	0.0	-	1.0	0.11 ± 0.03
$E=1.6\text{MeV}$, $N=10^{14}$	0.44 ± 0.02	2.33 ± 0.3	0.52 ± 0.02	0.50 ± 0.1	0.04	***
$E=1.6\text{MeV}$, $N=10^{15}$	0.0	-	0.0	-	1.0	0.63 ± 0.03
$E=1.6\text{MeV}$, $N=3 \times 10^{15}$	0.0	-	0.0	-	1.0	0.19 ± 0.01

*The h_a , h_b and h_p thicknesses are normalized to the total thickness of the sample.

**Errors of the calculated parameters have the following statistical meaning: if a given parameter is changed in the range of an error value, the 100% increase of the chi-square minimalization function will occur.

*** χ is negligible in the used H_{\perp} range.

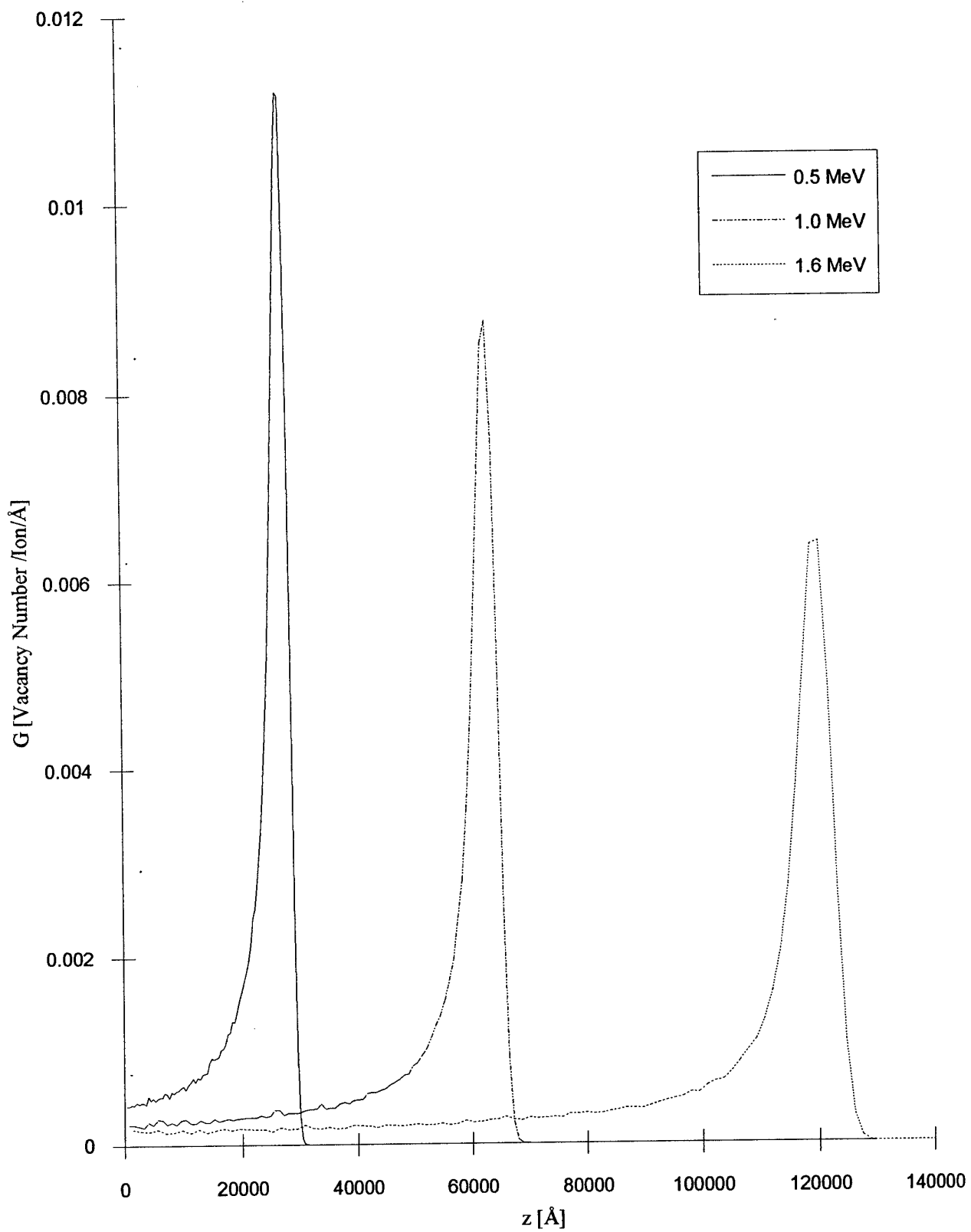


Fig.1. D^+ irradiation defect density profiles $G(z)$ versus depth z in garnet material as used for TF-MG production.

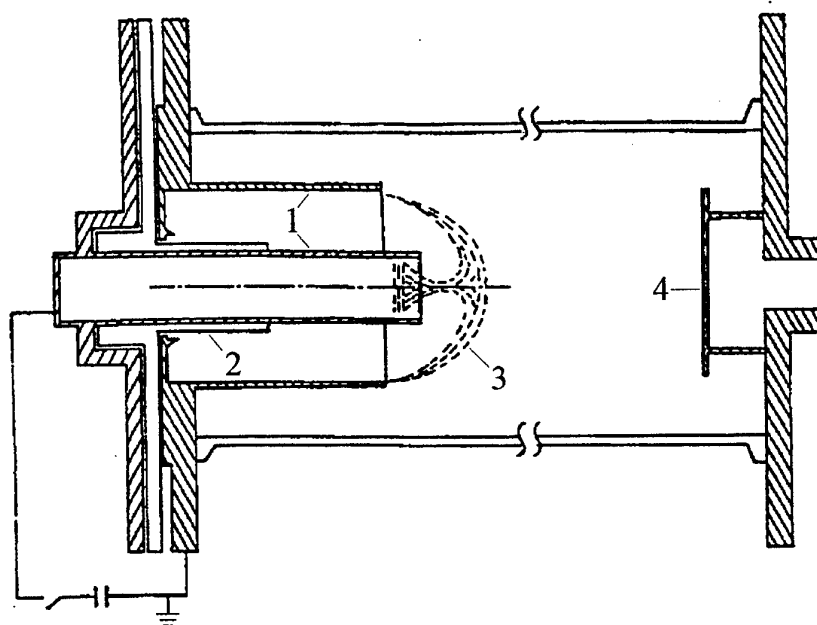


Fig.2. Experimental set-up for detection of the PDERs (produced during PF discharges) on impact with the TF-MG. (1) PF coaxial electrodes, (2) insulator, (3) symbolically marked position of the plasma pinch, (4) position of the TF-MG.

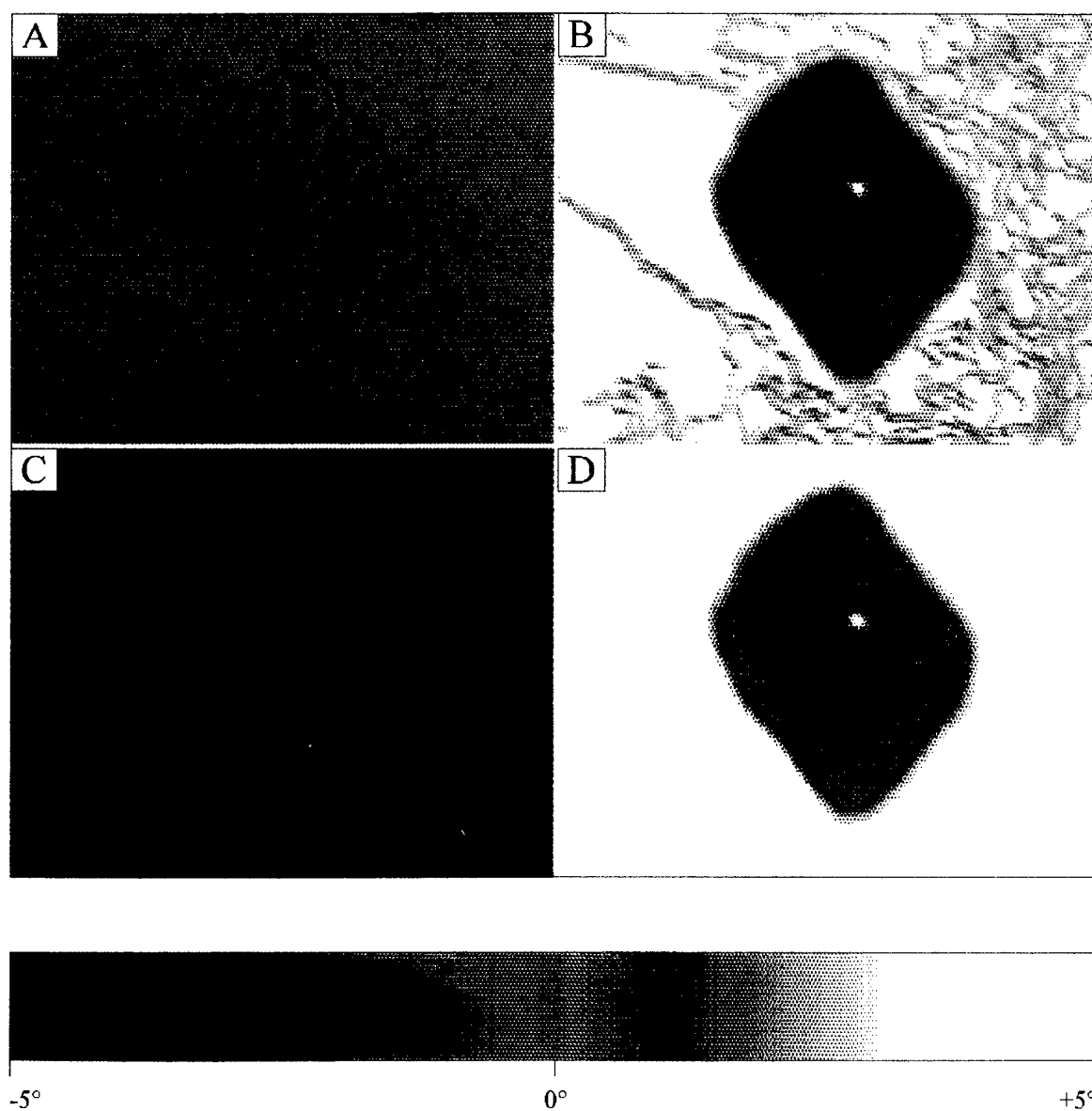


Fig.3. Illustration of the Faraday rotation method of visualization of ion defected region (Ref.[21], Apendix 4). Spatial distribution of Faraday rotation of TF-MG obtained for the region of D^+ implantation with $N=3 \times 10^{15}$ and $E=0.5$ MeV. Images were registered at different values of magnetic field H_{\perp} :

- A) $H_{\perp} = 0$, (after demagnetization),
- B) $H_{\perp} = +40$ Oe,
- C) $H_{\perp} = -80$ Oe,
- D) $H_{\perp} = +80$ Oe.

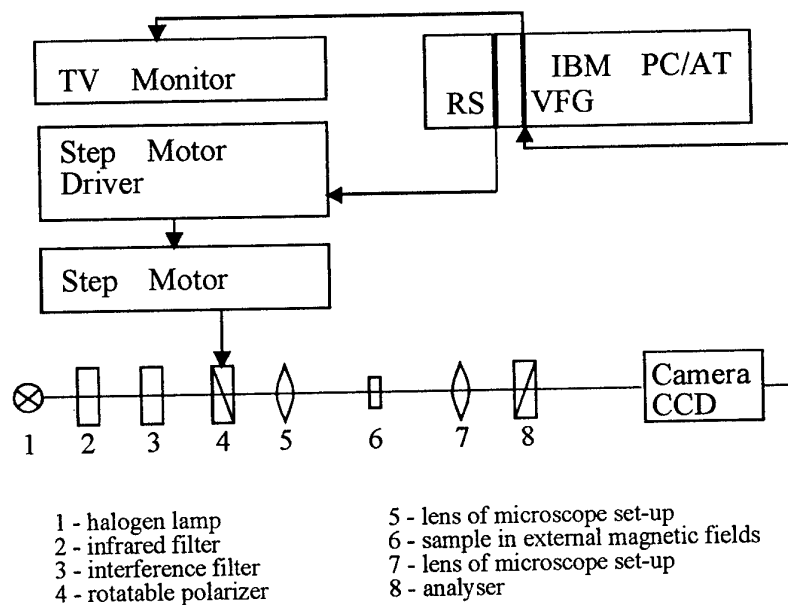
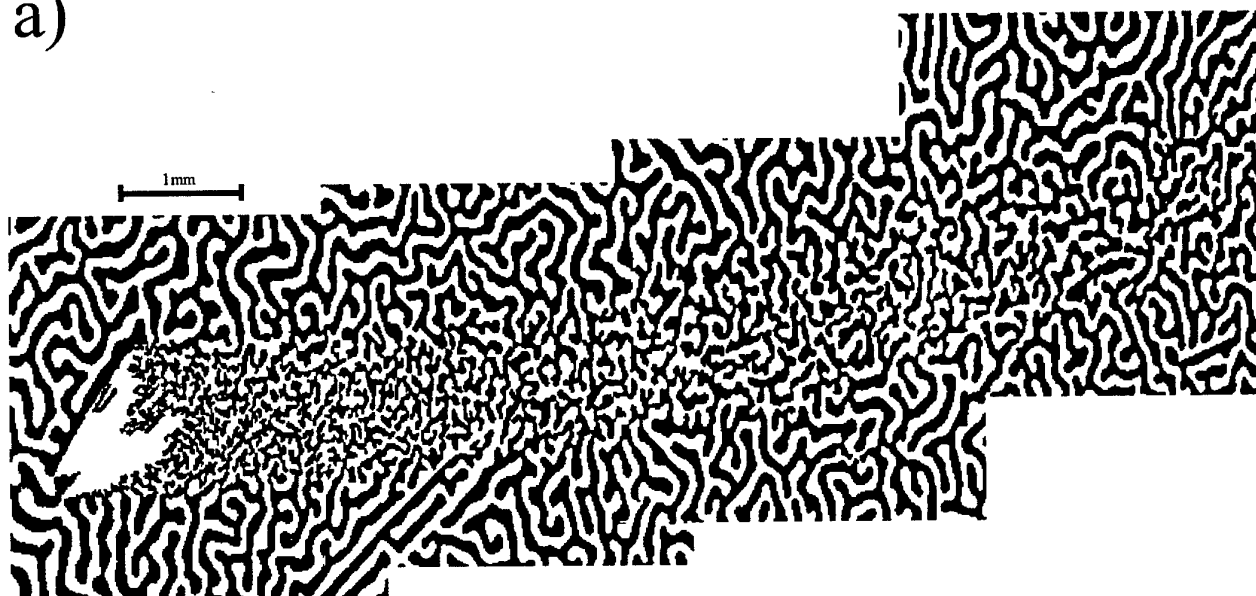


Fig.4. Imaging system used to visualise PDERS.

a)



b)

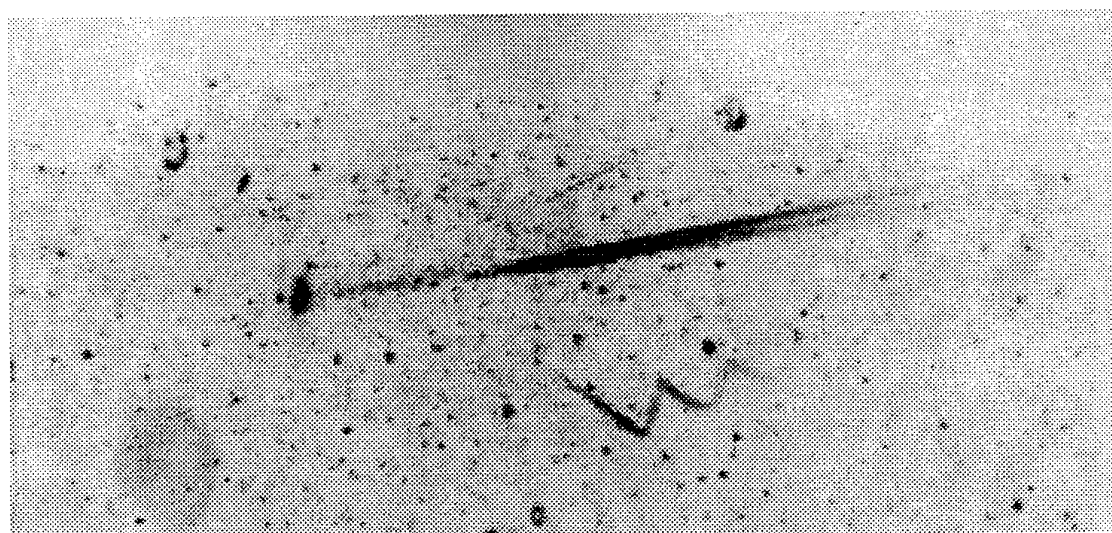


Fig.5. The images of the PDER recorded by TF-MG and visualised in transient light for magnetic treatment chosen in the way that maximum gradient in the domain wall length is achieved depending on density of ion deposition (a), and a similar PDER recorded with CR-39 track detector (b)

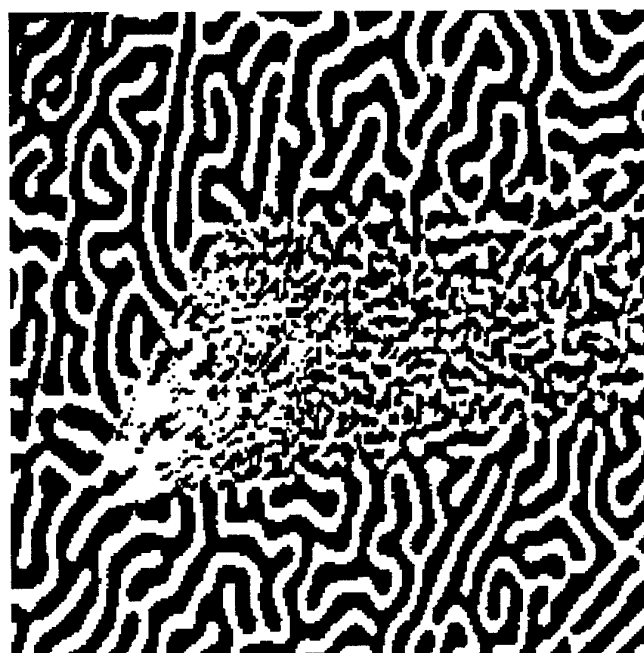


Fig.6. The major part of the PDER finger-print on TF-MG visualised after the sample had been demagnetized by $H_{\perp ac}$ alternating magnetic field with the amplitude decreasing from 200 Oe down to 0 Oe.

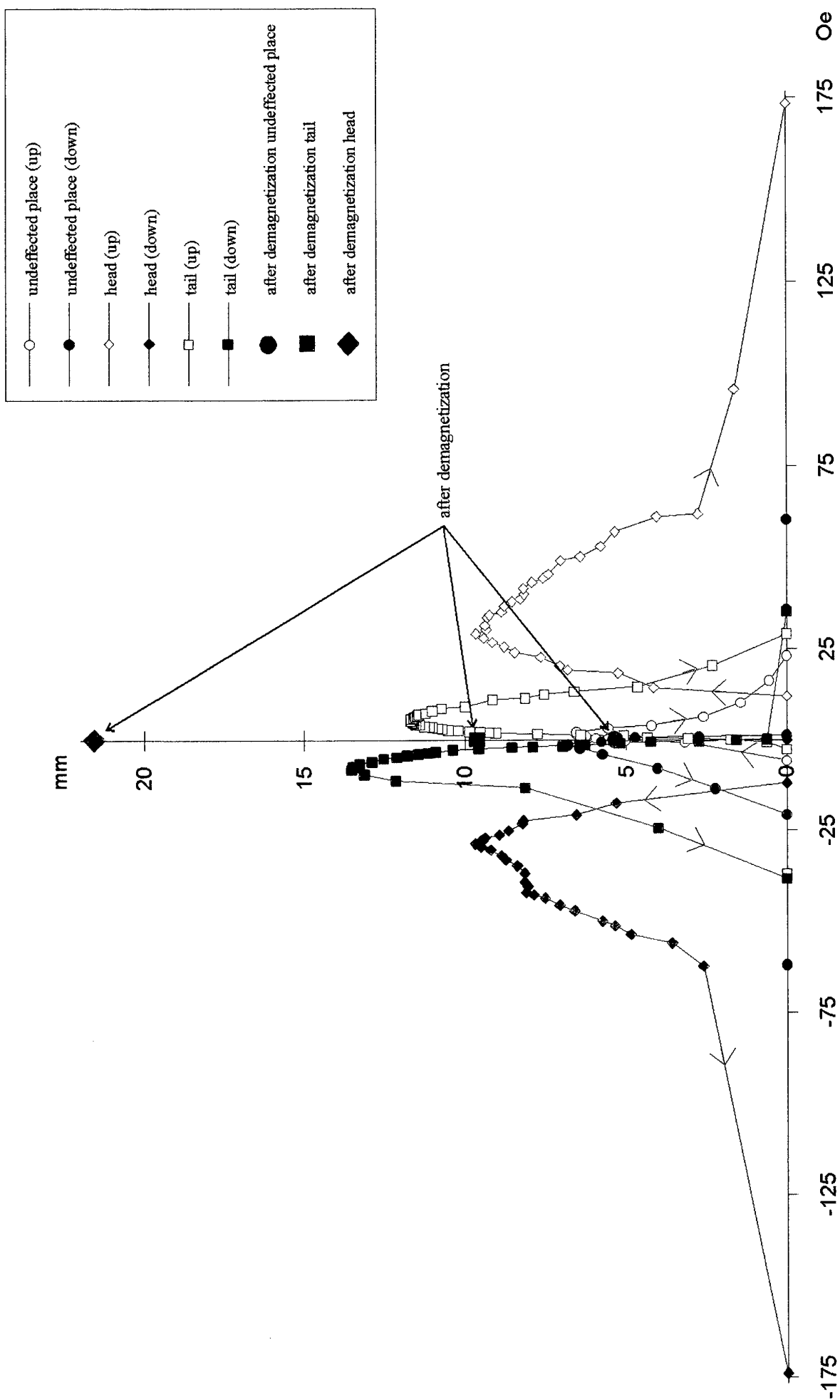


Fig.7a. Dependences of the domain wall length L as a function of the magnetic field H_{\perp} .

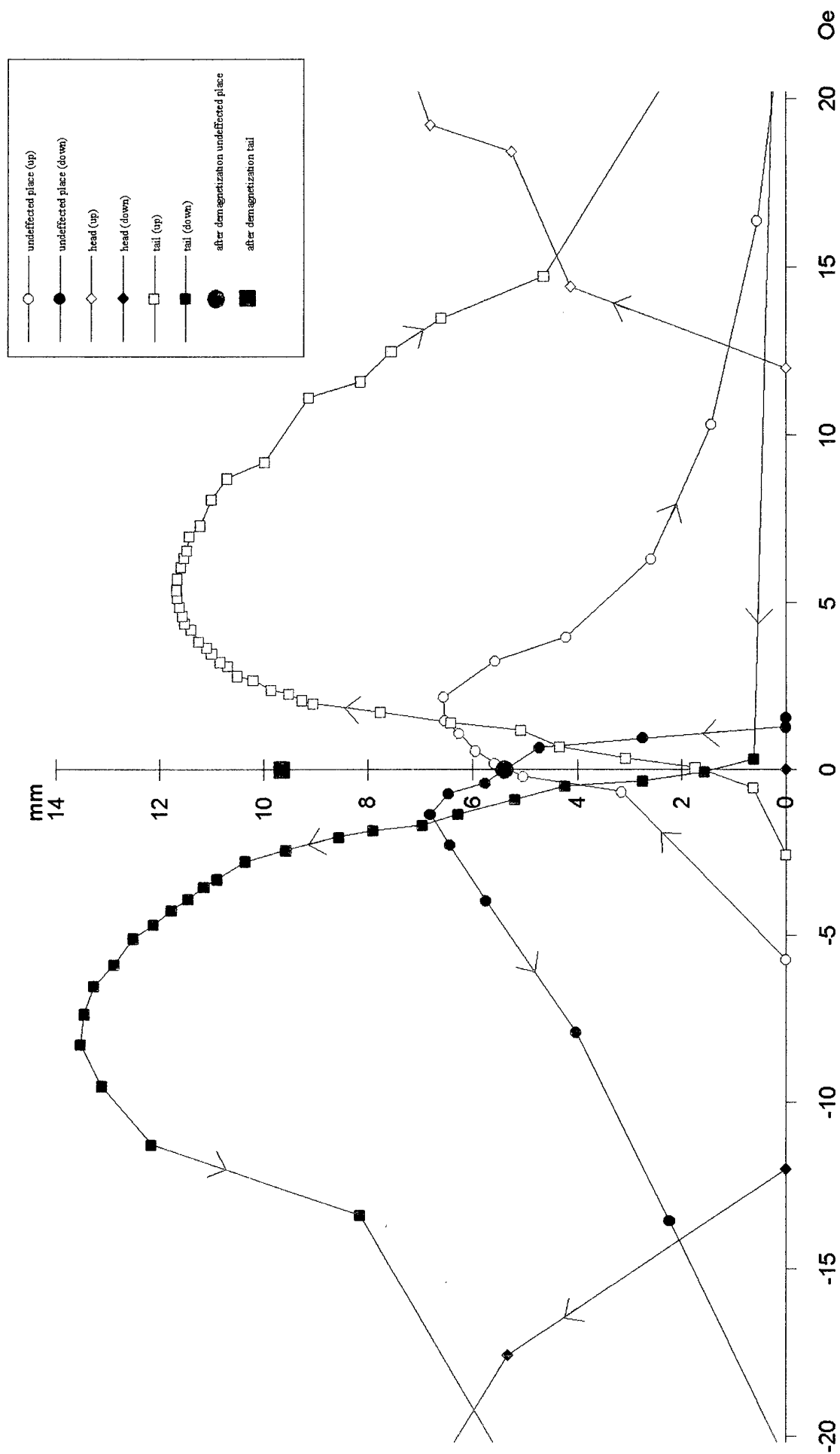


Fig.7b. Dependences of the domain wall length L as a function of the magnetic field H_{\perp} - magnified part of Fig.7a.

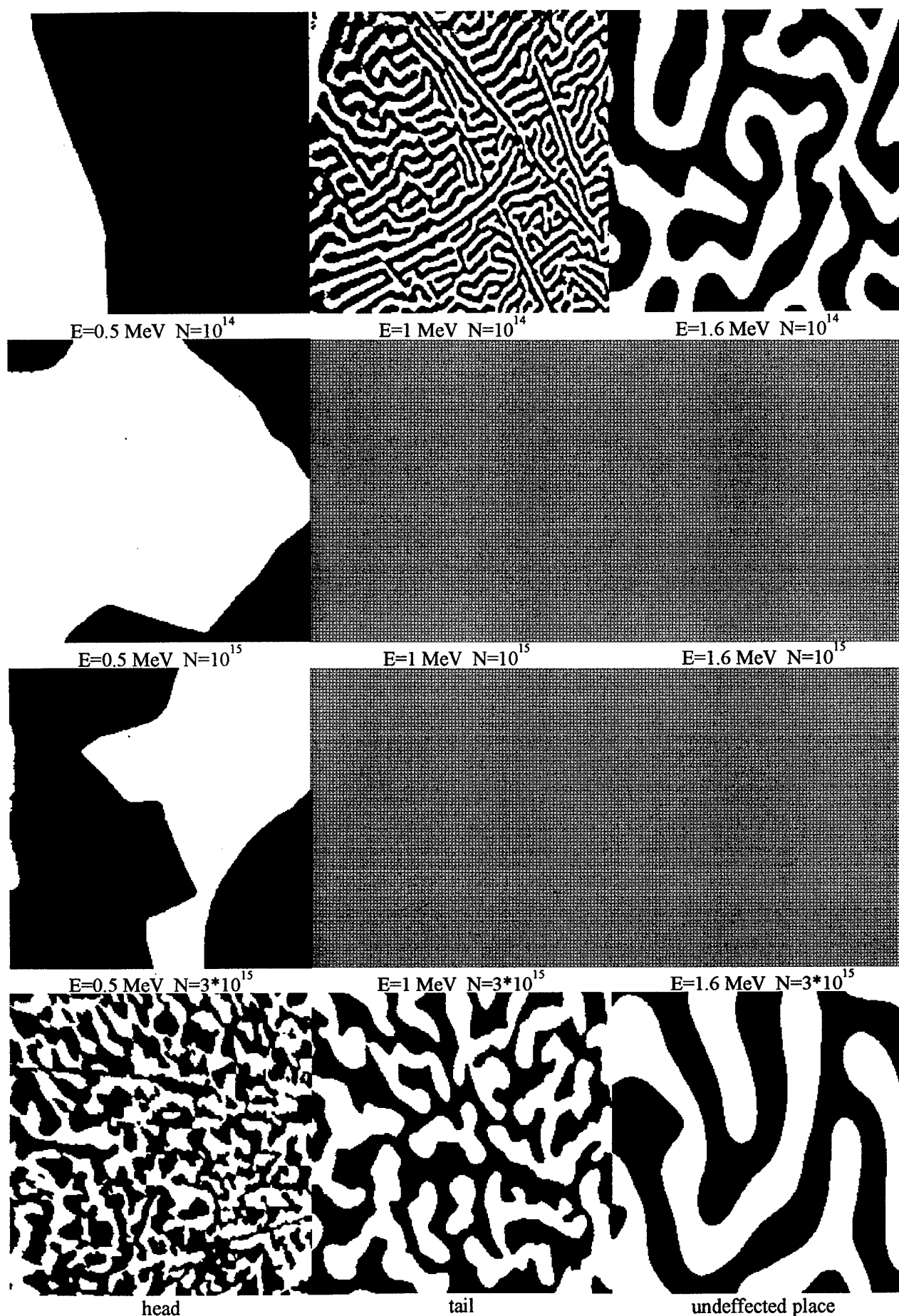


Fig.8. Domain structure magnified images obtained for plasma cluster trace area and implanted samples.

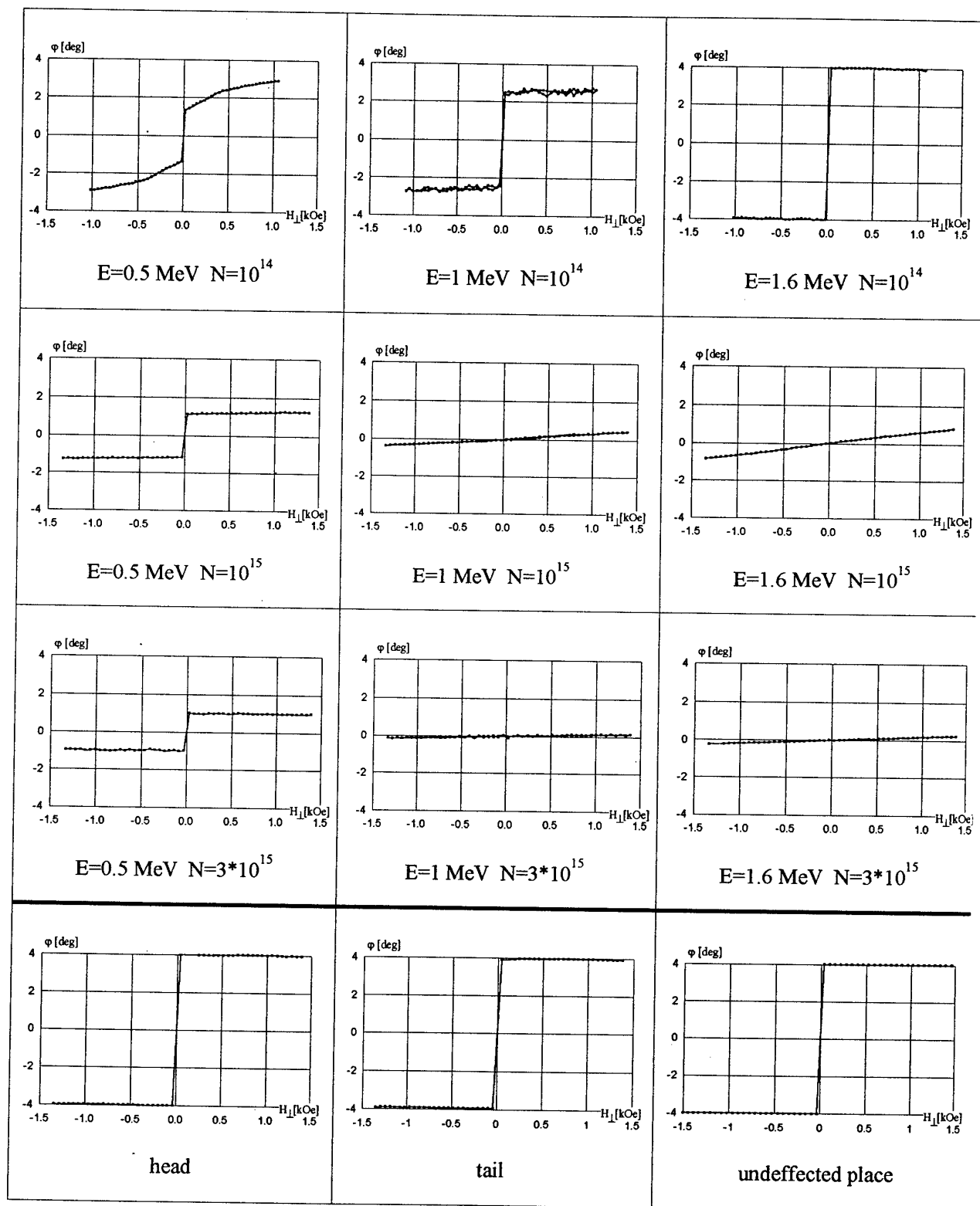


Fig.9. Faraday rotation $\phi(H_{\perp})$ measured for implanted areas and the PDER area. (E - energy, N - dose parameters are written inside the figure).

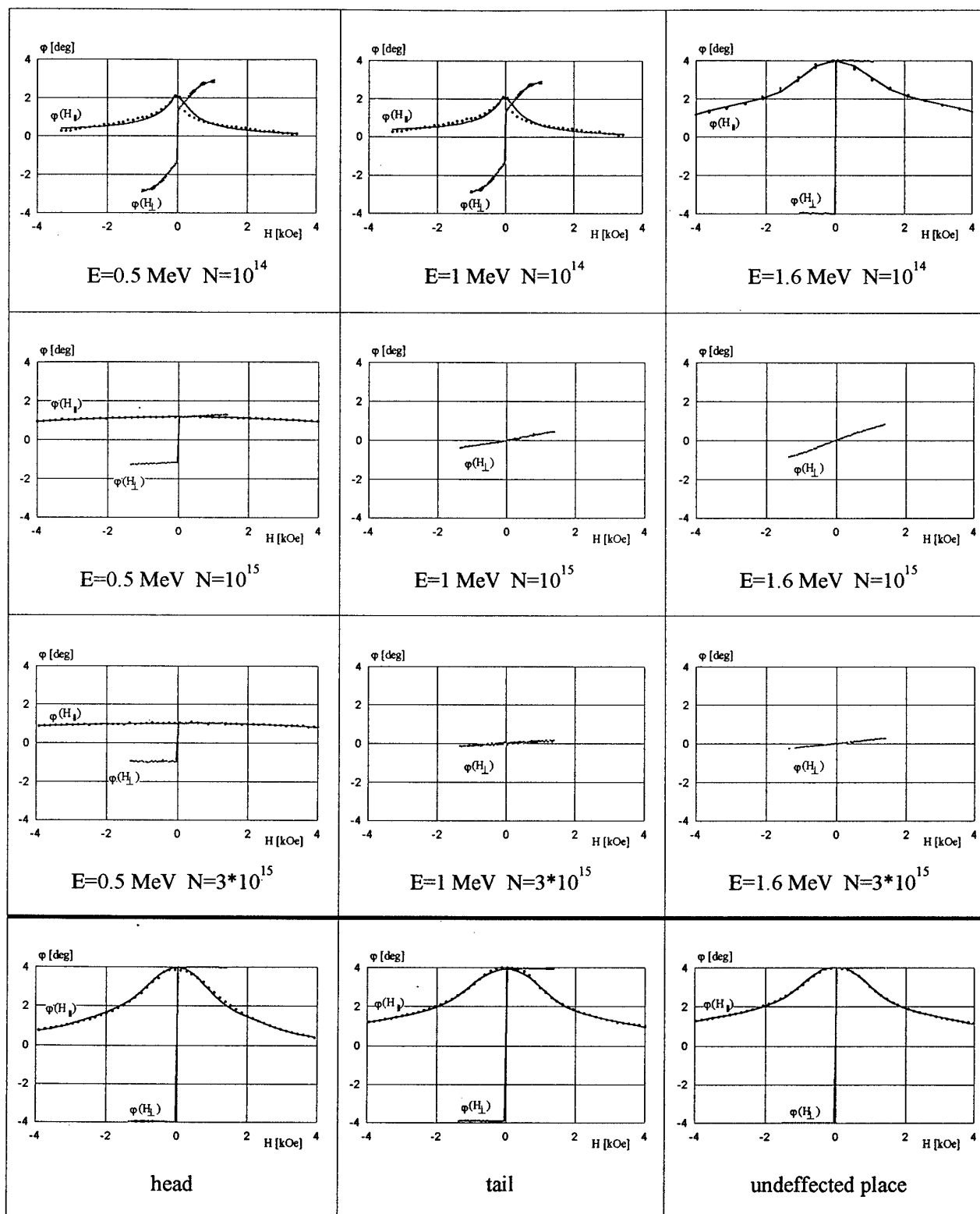


Fig.10. Faraday rotation $\phi(H_{||}, H_{\perp})$ measured for implanted areas and the PDER area (E - energy, N - dose parameters are written inside the figure).

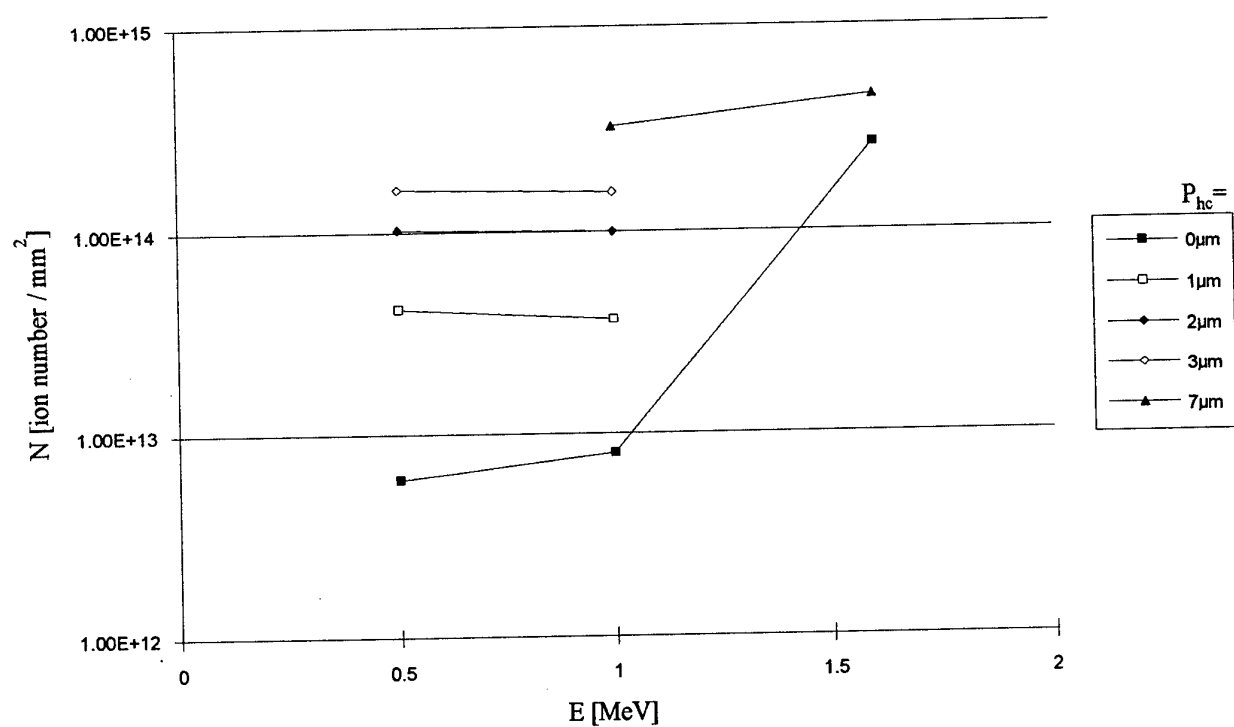


Fig. 11. Diagram $p_{hc}(E, N)$ of constant value of paramagnetic sublayer thickness constructed for $7\mu\text{m}$ -total-thickness-sample.

DETECTION OF PLASMA CLUSTERS WITH
THIN MAGNETIC FILMS
Technical Feasibility Study
First quarterly progress report
Special Project No. SPC-93-4022

Andrzej Maziewski
Warsaw University Branch
41 Lipowa Street
15-424 Bialystok
POLAND

7 July 1993

Abstract

This first partial report presents a brief summary of the introductory stage of the contract realization. Section 1 contain a description of the special magnetooptical stand which can be used for global, as well as microscopic investigation of magnetic garnet films. Such arrangement gives the possibility of quick initial checking of film surface with detailed investigation of the most interesting fragments to follow. The system includes the image processing part, that is controlled by a specialized software. Its main body is described in Section 2, which also contains some examples of its usage. The Section 3 consists of conclusions and remarks connected with the next stages of the contract realization.

1 Magneto-optical Stand for Magnetic Films Investigation

The main idea of the project is to use magnetic garnet films as plasma clusters detectors. It requires the investigation of a wide spectrum of magnetic material properties, as the interaction between the clusters and the films can be predicted only approximately. It has been shown over many years that the magneto-optical technique is the most powerful and flexible one, specially combined with the digital image processing (DIP). It allows to study many important properties of magnetic materials including

- magnetic anisotropy constants [1],
- magnetic susceptibility [2]
- magnetization value and direction, even within domains [3, 4, 5],
- domain structure parameters [6],
- dynamic parameters [7],
- magneto-optical and optical constants [8].

Moreover magneto-optical technique is non-destructive and can be arranged to investigate local as well as global characteristics.

Taking into account all the above merits the magneto-optical stand, presented on Fig.1, has been chosen as the basic tool in our study. The system is mainly prepared for static (or quasi-static) measurements in transmissive configuration (Faraday effect). However some new solutions were applied in comparison to standard systems of this type [5]. It was connected with the size of the samples under investigation (2-3 inch diameter is considered as typical in order to obtain high probability of cluster impacts).

The special sample holder is integrated with the perpendicular field Helmholtz coils. The holder assures repetitive positioning of large sample. The coils allow to put static (up to 500 Oe) and alternating (up to 100 Oe) fields to the sample and makes it possible to change the field of view in wide ranges (up to 5 cm diameter). The device is placed between poles of the electromagnet, which is the in-plane field (up to 4 kOe) source.

The optical path of the system consists of changeable light source (halogen lamp, CW or pulse laser), collimator or beam expander, polarizer (that optionally can be placed in rotating holder for modulation technique [3] application), projecting optics with analyzer and CCD camera. The projecting part has two arrangements:

- simple projecting lens (the active field of view 1.5x2.0 cm, resolution better than 0.1 mm),
- optical microscope system (resolution up to 1 μ m).

This solution allows to use the stand in two modes. We have planned to use the first one for initial sample characterization and detecting changes after plasma focus irradiation, the second one will be used for detailed investigation of detected cluster impacts.

The TV camera (common CCD - *Mintron 1801CB* or asynchronous *EEV P46582*) is a part of the DIP system which also contain PC/486 computer (8 MB RAM, HD 600 MB), frame grabber *Visionetics VFG512-8BC* (resolution 512x512, 8 bit, pseudocolor), video recorder *NEC PC VCR*, printer *HP IIP*, monitors etc. This part of the system is driven by the special software described in Section 2.

2 Digital Image Processing Software

From the very beginning of the project foundation it was assumed that its realization would be intensively supported by DIP technique. Many DIP methods had been mastered and checked earlier, but it was obvious that their efficient maintenance required a new powerful software that would cope with all necessary procedures. Commercial programs of this type were rather expensive and usually not flexible enough, so the software was created in Bialystok, specially for the contract realization.

Its creation was based on the following assumptions:

- wide flexibility, that should ascertain the possibility of adding and exchanging all functions,
- hardware independence, which means that the program should easily work with arbitrary PC equipment (computer, graphic adapter, printer etc.),
- user-friendly interface.

The attached program seems to fulfill all the above requirements. The source code has been written in *Borland's TURBO PASCAL v.6.0* with *TURBO VISION* library use. Some *TURBO ASSEMBLER* parts have been included in order to increase the program efficiency. The pull-down menus and mouse interface make it user-friendly and easy for learning. It can be run with or without the frame grabber. Its adaptation to virtually all graphic adapters and printers (using *PIZZAS* interface) is also very simple. The attached version contains the basic functions only, but some specialized optional blocks are ready and can be included at any time, if it is necessary (e.g. advanced geometrical analysis [6], Fourier analysis [9] or image library service). Taking into account the memory limits and processing time, initially the program operates on image quarters (256x256 pixels). There are reserved two 64 kB RAM blocks for source and result image storage.

The basic version of the program requires a PC/AT computer (1 MB RAM, FD 5.25', SVGA 1 MB and SVGA monitor) as the minimal configuration. Optionally it can work with other devices (frame grabber, camera, TV monitor, video-recorder, mouse, printer etc.). It includes the following functions:

Input - image reading from the file or the frame grabber. The input image can be averaged by multiple addition.

Filtration - different filtration procedures (finite impulse response [10], directional [11] or median [12]).

Calculation - basic calculating procedures [11] (automatic and manual histogram optimization).

Comparison - simple correlation procedure [6].

Analysis - basic geometrical and statistical operations [11, 3, 6] (image fragmentation, boundaries indication, simple measurements).

Output - basic output functions (frame grabber control, image transfers, printing etc.).

The main panel is shown on Fig.2. It contains the main menu and the real time clock at the top and the secondary menu and the free memory space index at the bottom. All the functions are easily accessible by pull-down menus (see Fig.3) and conversation windows (see Fig.4). The exemplary print-outs, presenting selected software possibilities, are shown on Figs. 5-10.

3 Conclusions

The prepared hardware and software equipment is planned to be used for preparing the documentation of selected samples. The comparison of the initial and final states should detect the influence of the processing (implantation or plasma focus irradiation). Then the observed changes would be investigated in detail.

The investigation method will be fully tested in the next stage during the implanted samples study. It should allow for making all the necessary changes (e.g. more advanced automatization or software complement) before plasma cluster irradiation experiment.

References

- [1] A.Maziewski, A.Stankiewicz, M.Tekielak, V.V.Volkov, "Magneto-optical anisotropy of magnetic garnet films", *Fiz. Niz. Temp.*, 18-S1 (1992) 371.
- [2] M.Kisielewski, A.Maziewski, "AC susceptibility analysis of YIG+Co films", *Acta Phys. Pol.*, A76 (1989) 283.
- [3] E.Kubajewska, A.Maziewski, A.Stankiewicz, "Digital image processing for investigation of domain structure in garnet films", *Thin Solid Films*, 175 (1989) 299.
- [4] A.Maziewski, "Unexpected magnetization processes in YIG+Co films", *JMMM*, 88 (1990) 325.

- [5] M.Marysko, A.Maziewski, A.Stankiewicz, M.Tekielak, V.V.Volkov, "Magnetic anisotropy investigation in (210)-oriented Bi-substituted magnetic garnets", Phys. B, in press.
- [6] A.Maziewski, K.Mroczek, A.Stankiewicz, M.Tekielak, M.Kisielewski, "Digital image processing application for magnetooptical domain structure investigation", Fiz. Niz. Temp., 18-S1 (1992) 377.
- [7] B.A.Ivanov, A.Stankiewicz, A.Maziewski, N.L.Petrichenko, K.A.Safaryan, "Magnetic domain mobility investigation in in-plane field", *Proc. of ICF 6 Conf.*, Tokyo (1992) .
- [8] A.Paoletti (ed.), *Physics of Magnetic Garnets*, North-Holland Publ. 1978.
- [9] E.Kubajewska, A.Maziewski, A.Stankiewicz, "Domain structure analysis in garnets by digital image processing", Acta Phys. Pol., A77 (1990) 705.
- [10] D.E.Dudgeon, R.M.Mersereau, *Multidimensional Digital Signal Processing*, Prentice-Hall 1984.
- [11] T.Pavlidis, *Algorithms for Graphics and Image Processing*, Computer Science Press, 1982.
- [12] S.Barua "Finite impulse response - median hybrid filtering techniques for image smoothing", Opt. Eng., 30 (1991) 271.

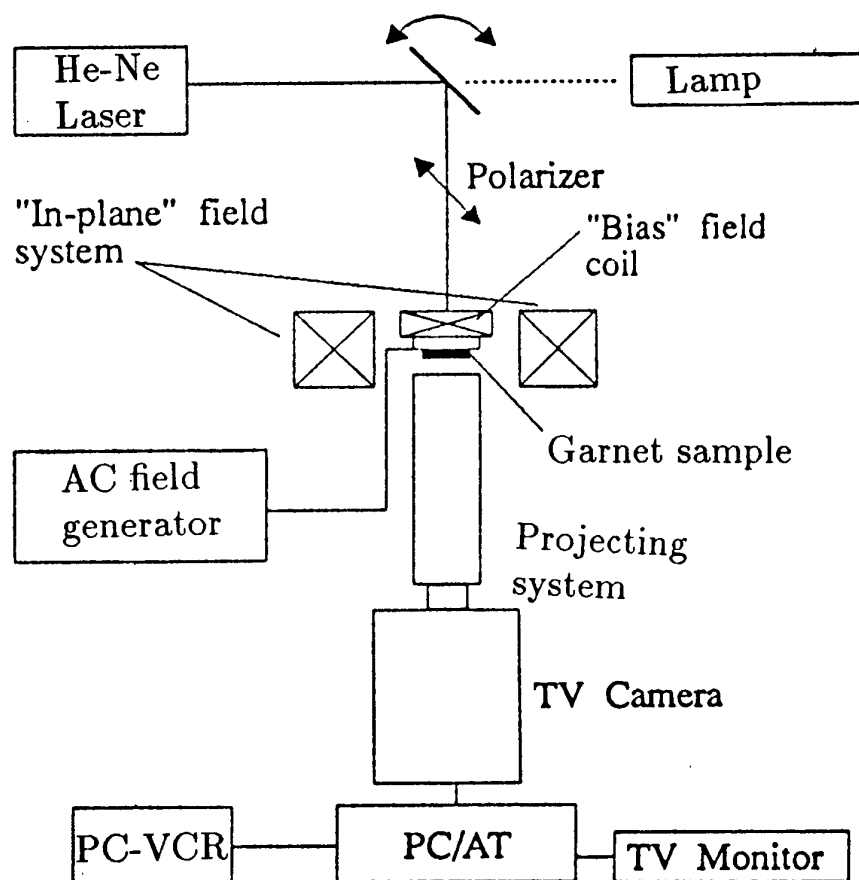


Figure 1: The measurement system

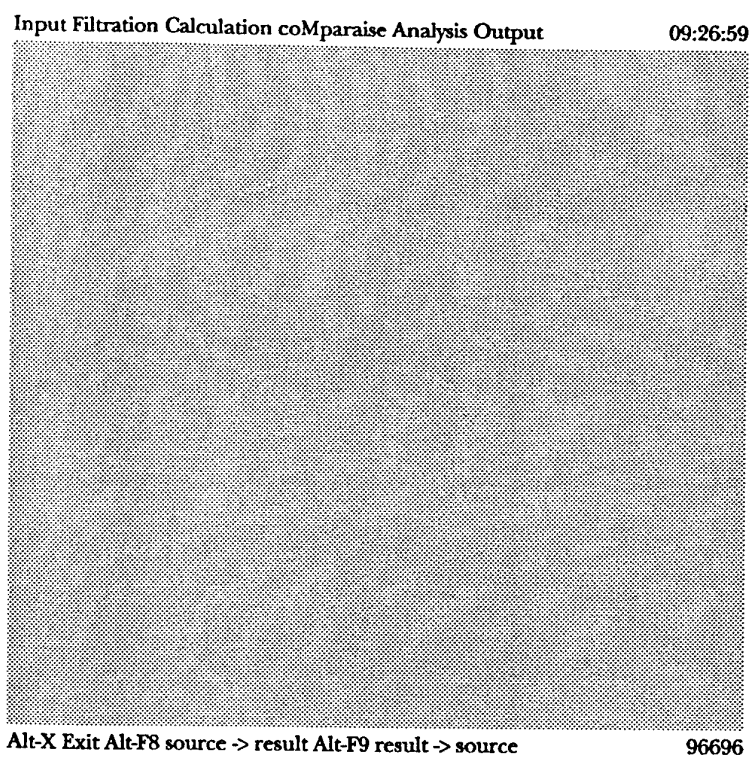


Figure 2: The main panel of the software

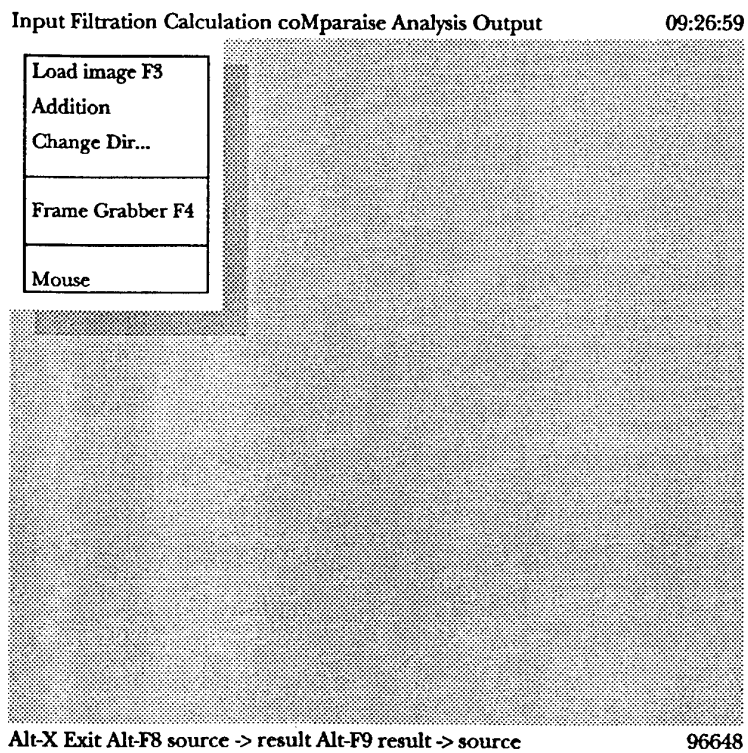


Figure 3: The pull-down menu

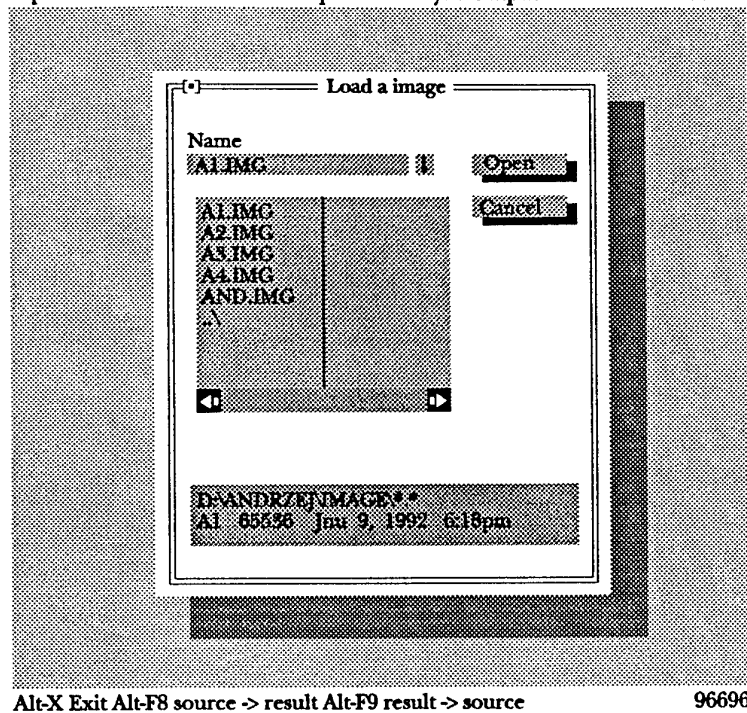
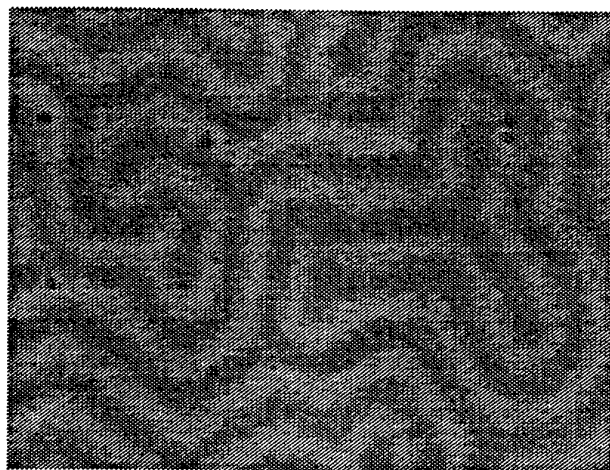


Figure 4: The conversation window



AA01.OBR 19.2.1993 18:39:0

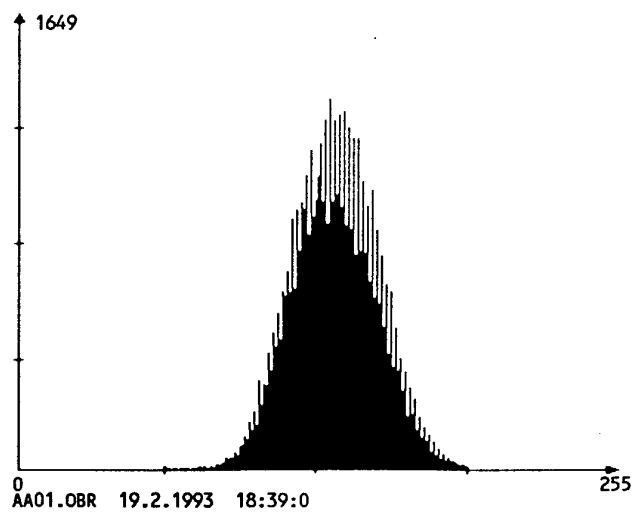
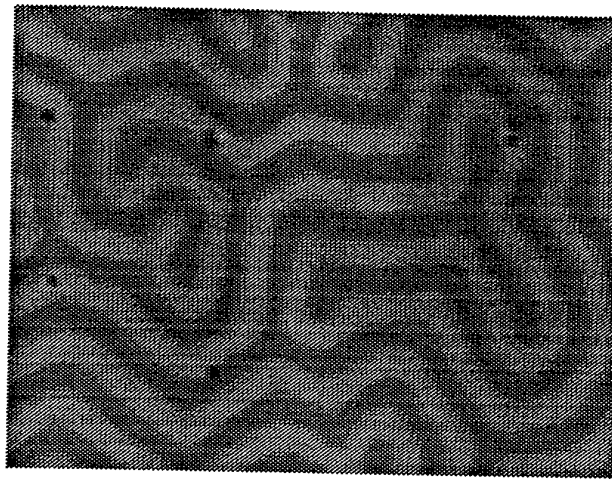


Figure 5: The original image of domain structure and its histogram



AA03.OBR 4.2.1993 10:25:10

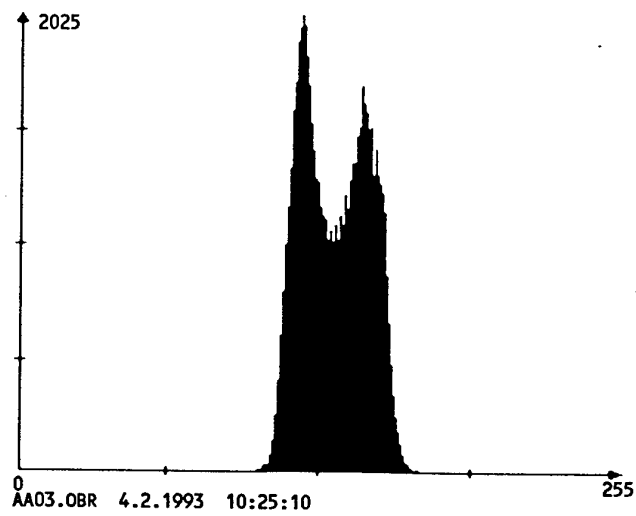
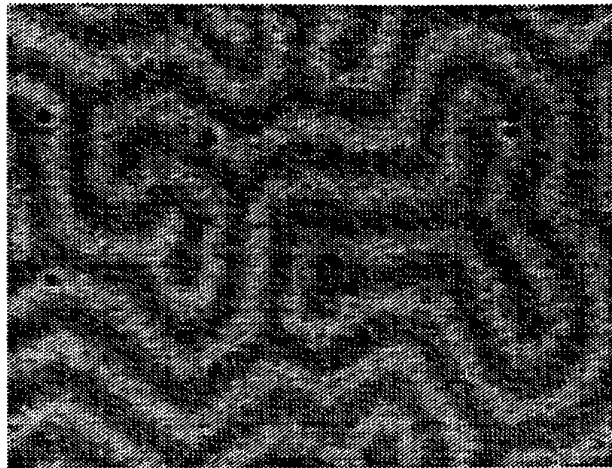


Figure 6: The image after 100-times averaging and its histogram



DD01.OBR 25.2.1993 12:27:14

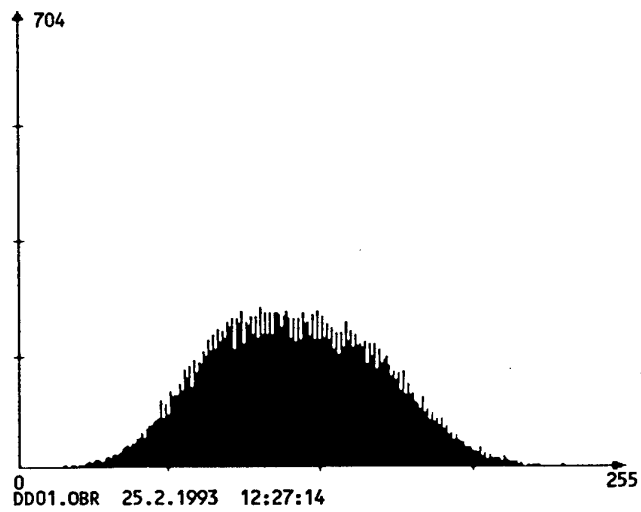
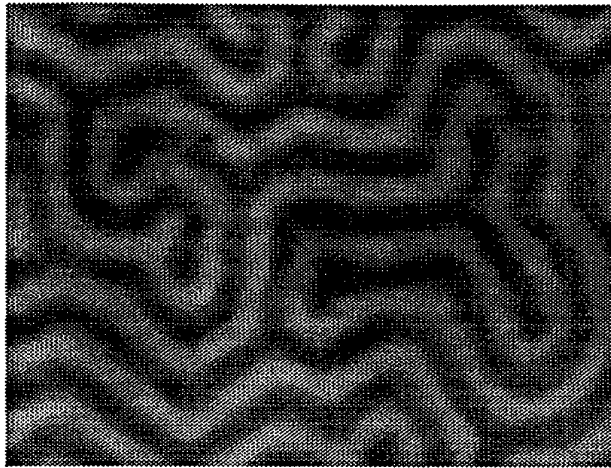


Figure 7: The image for median filtering



DD03.OBR 25.2.1993 12:34:0

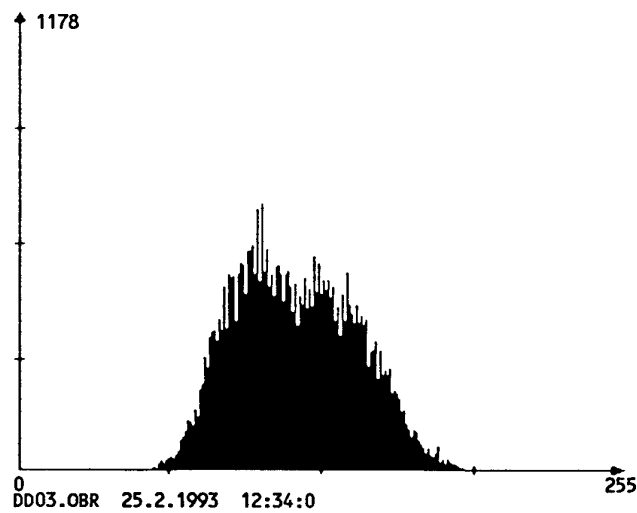
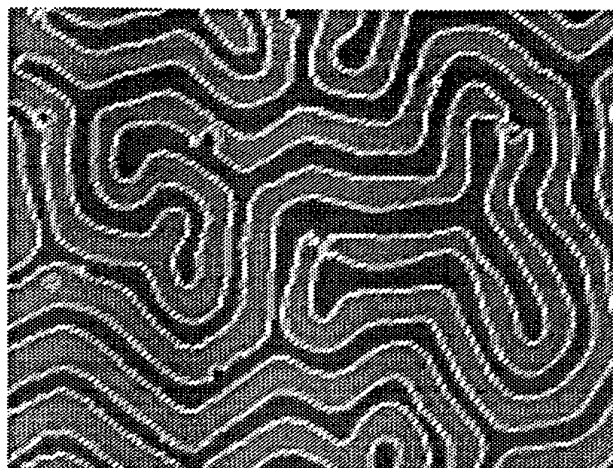


Figure 8: The image from fig.7 after median filtering



EE04.OBR 25.2.1993 10:40:2

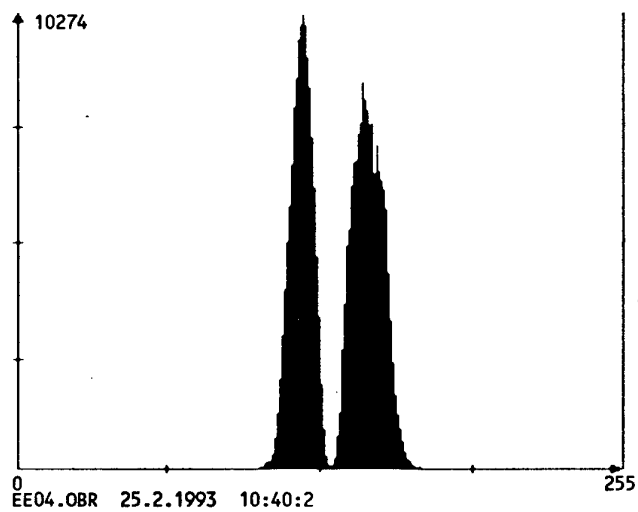
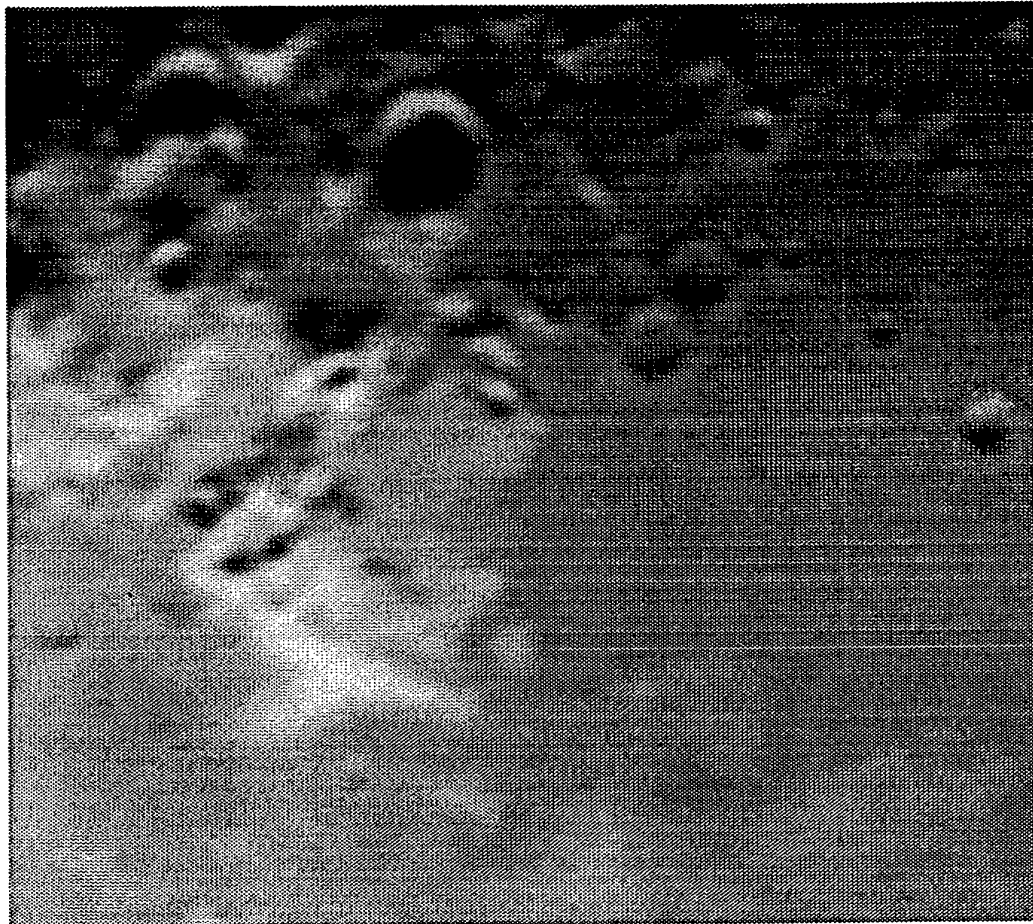


Figure 9: The border detection



KS1. 7.1.1993 9:54:26

Figure 10: The moon surface registered on the magnetic tape and then processed by the software

DETECTION OF PLASMA CLUSTERS WITH
THIN MAGNETIC FILMS
Technical Feasibility Study
Second quarterly progress report
Special Project No. SPC-93-4022

Andrzej Maziewski
Warsaw University Branch
41 Lipowa Street
15-424 Bialystok
POLAND

7 October 1993

Abstract

The second quarterly progress report presents initial simulations of a plasma cluster impacts on magnetic garnet thin film surface. As probably the clusters consist mainly of deuterium, a deuterium beam (of particle energy 0.5 MeV) was used as the stimulating agent, causing its implantation to the magnetic layer surface. Two samples with quite different initial properties (one of easy-axis anisotropy and another of easy-plane anisotropy) were processed so far. Optical (e.g. absorption), magnetooptical (e.g. Faraday rotation) and magnetic (e.g. anisotropy) changes were detected and measured for both samples using magnetooptical method. It was stated that a degree of these changes is strongly dependent on the implantation dose ranging from 10^{13} to 10^{15} ions/mm².

1 Implantation effects

When a crystal surface is implanted with a well chosen light ion type, dose and energy, the implantation causes changes of a crystal lattice in the surface layer [1]. These changes are usually of two types:

- placing implanted ions in interstitial positions (this may cause additional strains or crystal expansion, influencing related parameters) [1, 2, 3, 4],
- introduction of defects, sometimes ranging to full crystal structure destruction or modification [4, 5, 6, 7].

In case of a magnetic thin film this can have effect on all global characteristics of the material under investigation, including:

- optical constants [8] (e.g. absorption, refracting index tensor),
- magnetic characteristics [4, 9] (e.g. magnetization, anisotropy),
- magnetooptical constants [10, 11] (e.g. Faraday or Kerr rotation).

The most spectacular effect of ion implantation is a change in magnetic anisotropy [3, 4, 5, 7] resulting from changes in the lattice constant perpendicular to the film plane and local damage to the crystal structure. Kamenou et al. [3] showed that the so called non-magnetic region could be created in the implanted layer when the dose exceeded some critical value.

The effect of local light ion implantation can be expected after plasma cluster impact. In this study the deuterium implantation was investigated in the magnetic garnet films in order to check the possibility of local implantation detection and quantitative evaluation. As compared to all other implant elements, deuterium leads to the largest anisotropy changes [4, 7] and it has rather deep penetration, so it turned out to be the most convenient starting point for research.

2 Magnetic garnet films

To select the material for investigation, a few conditions had to be taken into account from the start:

- sensitivity to factors that are probably present in plasma clusters,
- cost effectiveness and easy availability (including well developed, repetitive production technology),
- the possibility of local area, time effective investigation.

It seems that the above requirements are well fulfilled by thin magnetic garnet films. Garnets are generally cubic crystals containing three sublattices. The films used in this study are rare earth (RE) iron garnet of formula $\{RE_3\}[Fe_2](Fe_3)O_{12}$ where {}, [] and () stand for dodecahedral (c), octahedral (a) and tetrahedral (d)

sites, respectively. Ferrimagnetic garnet films were grown by liquid phase epitaxy method on a paramagnetic $Gd_3Ga_5O_{12}$ substrate. Samples of this kind were used for model investigation of magnetic and magneto-optical properties for many years [12], so the previous knowledge should help in the interpretation of plasma clusters influence on them. They are rather cheap and have well developed technology. Additionally, its magneto-optical properties allow to investigate them by non-destructive local methods in both transmissive (Faraday) and reflective (Kerr) configurations. The Faraday configuration [10] has been used for this report preparation, as it is simpler and more time effective than the Kerr case.

Usually the thickness h of magnetic garnet films is known from the production process. The magneto-optical method [13] enables local measurement of the following characteristics of thin magnetic garnet films:

- optical absorption α ,
- Faraday rotation φ (proportional to the mean perpendicular component of magnetization),
- domain structure period p .

Assuming the presence of domain structure in absence of external field and taking into account that the mentioned parameters can be measured in dependence on external field vector, one can estimate virtually all magnetic properties of the sample including:

- characteristic length l [14],
- saturation magnetization M_s [15],
- anisotropy constants (e.g. K_u — uniaxial anisotropy constant) [15, 16],
- exchange constant A .

For the simplest case of pure uniaxial film the quality factor Q is defined as

$$Q = \frac{H_u}{4\pi M_s}$$

where $H_u = 2K_u/M_s$ — anisotropy field.

In case of $Q > 1$ there is a unique easy axis (usually perpendicular to the film plane), $Q \leq 0$ corresponds to easy plane anisotropy. The case of $0 < Q < 1$ is mixed situation as the magnetization tends to in-plane position, however demagnetization energy decrease may be also obtained by some domain structure formation. $Q = 1$ leads to full frustration of the system by anisotropy and demagnetization energies compensation.

When $Q > 1$ the film usually possesses some domain structure and the characteristic length l can be evaluated from p in demagnetized state using the method described in [14]. M_s can be estimated e.g. $\varphi(\vec{H})$ dependencies [12]. Then one can derive A using the formula:

$$l = \frac{\sigma_w}{4\pi M_s^2}$$

where $\sigma_w = 4\sqrt{AK_u}$ — domain wall energy per unit area.

Many properties of magnetic garnet films can easily be controlled by changing technological conditions. For reducing the magnetization non-magnetic diluents such as gallium or germanium are added, which replace preferentially iron ions on d sites. K_u is usually derived from two mechanisms: a growth-induced anisotropy K_g (possible control by annealing) and a stress-induced anisotropy K_s (possible control by chemical content changes).

3 Experiment

The garnets used in the present case were selected from the series of different compositions and the properties:

Film 1 — with the large uniaxial anisotropy perpendicular to the film plane,

Film 2 — with the easy plane anisotropy type.

Investigations were carried out on 3-in-diameter garnet films which were grown by standard liquid phase epitaxy method on [111]-oriented gadolinium – gallium garnet substrate. The garnet compositions were $Bi_{0.8}Tm_{2.2}Fe_{3.9}Ga_{1.1}O_{12}$ for the film 1 ($h=6\mu m$) and $Bi:YIG$ for the film 2 ($h=5.5\mu m$).

In this study we present the results with deuterium implantation doses ranging from 10^{13} to 10^{15} ions/mm² at implantation energy 0.5 MeV. Similar values may be expected in plasma focus irradiation [17]. The implanted area of approximately rectangular shape was found to be about 1×1 mm². Before implantation, the garnet was covered by an uniform 0.1 μm aluminum layer.

In case of the film 1 (film 2, as easy plane sample, lacks domain structure), Faraday rotation was used for producing geometrical image of domain structure in the optical polarizing microscope. The image was registered by CCD camera and, in real time, digitized by a frame grabber connected to IBM PC. The magneto-optical stand for this investigation was presented in detail in [18]. The digital image processing software [18, 19, 13] was applied for quantitative evaluation of the implantation effects and results are presented in Table 1.

The first aim of our procedure was to detect implanted areas. It turned out to be very easy, because of absorption changes accompanying other effects. Fig.1 and Fig.5 show easily visible areas of implantation on both samples. The corresponding changes of domain structure for film 1 are well visible on Fig.2.

The Faraday rotation φ of the exploited sample was measured with the applied magnetic field perpendicular (H_{\perp}) and/or parallel (H_{\parallel}) to the sample, in the non-implanted and implanted area of the film. The measurements of each film were recorded before and after implantation (without any heat treatment).

In Fig.3 the variation of Faraday rotation φ as a function of perpendicular magnetic field is shown for film 1, implanted for three different doses at a constant energy.

Table 1: Parameters of unimplanted and implanted areas of film 1.

Dose ion/mm ²	p [μ m]	l [μ m]	$4\pi M_s$ [Gs]	K_u [erg/cm ³]	Q	A [10 ⁻⁷ erg/cm]	α [a.u.]	φ_{max} [deg]
0	40	1.5	92	7200	21	0.86	1.00	5.3
10 ¹³	42	2.4	63	5040	32	0.79	0.80	5.3
10 ¹⁴	88	3.8	21	1680	96	0.06	0.34	4.0
10 ¹⁵	96	4.0	15	1100	123	0.03	0.33	3.8

Fig.4 shows Faraday rotation φ versus in-plane magnetic field for film 1 (in presence of saturating bias field) implanted at three different doses of 0.5 MeV energy. Fig.6 and Fig.7 show analogous dependencies for film 2.

4 Discussion

Fig.1 and Fig.5 show that implanted areas are easily recognizable, even with the simplest optical equipment. The correlation images assure full resolution between regions of possible defects which could exist before processing and the very implantation effects. However the origin of absorption increase is not clear enough, it may be connected with some thermal interaction between the aluminum cover and the layer.

In case of domain structure existence (film 1) implantation may cause strong changes of geometrical parameters of domains, as it is presented on the Fig.2.

In Fig.3 and Fig.6 it is seen as a great decrease of Faraday rotation φ , and saturation magnetic field H_1 on implanted part of the samples as compared to the unimplanted parts. This is connected with the strong tendency of in-plane anisotropy to increase in the implanted layers [3, 4, 5, 7]. This anisotropy is caused via negative magnetostriction by an in-plane stress induced in implanted films.

For the film 2 (Fig.6) we found that Faraday rotation increased monotonically in the unimplanted and implanted parts of the sample with the applied perpendicular field. Probably that is due to the large anisotropy type easy plane in this sample.

Strong changes of the anisotropy fields are also visible on Fig.4 and Fig.7, presenting $\varphi(H_{||})$ dependencies for samples placed in the perpendicular field.

All the measured and calculated values should be interpreted as parameters averaged along the layer thickness. However implanted regions are usually unhomogeneous. Probably the reflective (Kerr) configuration would give more reliable results [11].

5 Conclusion

Deuterium implantation of magnetic garnet films can vary their important parameters of them, e.g. magnetic anisotropy, period of the domain structure and optical

absorption. The magnitude of these changes strongly depends on the ion doses used.

We have shown that the proposed procedure of investigation is a powerful technique for the analysis of different parameters distribution in garnet films and then, detection of the local incidents influence. A comparison of the initial and final values of the magnetic parameters should show the local influence of the plasma focus irradiation.

References

- [1] J.C.North and R.Wolfe, "Ion-Implantation Effects in Bubble Garnets" in *Ion-Implantation in Semiconductors and other Materials*, ed. B.L.Crowder, Plenum, New York 1973.
- [2] B.E.MacNeal and V.C.Speriosu, J.Appl.Phys., 52, 3935 (1981).
- [3] K.Kamenou, I.Hirai, K.Asama and H.Sakai, J.Appl.Phys., 49, 5816 (1978).
- [4] P.Gerard, Thin Solid Films, 114, 3 (1984).
- [5] V.S.Speriosu and C.H.Wilts, J.Appl.Phys., 54, 3325 (1983).
- [6] C.H.Wilts, H.Awano and V.S.Speriosu, J.Appl.Phys., 57, 2161 (1985).
- [7] C.H.Wilts and A.Urai, J.Appl.Phys., 64, 4633 (1988).
- [8] A.Algra and W.H. de Roode, J.Appl.Phys., 53, 5131 (1982).
- [9] A.Karpinski, A.Maziewski and J.Zytkowski, Sci. mat. Warsaw Univ. Branch Bialystok, 25, 89 (1980).
- [10] P.Hansen, H.Heitman and H.A.Algra, IEEE Trans.Magn., 19, 1769 (1983).
- [11] R.Krishnan *et al.*, IEEE Trans.Magn., 18, 1280, (1982).
- [12] P.Hansen *et al.*, Landoldt-Börnstein, New Series, vol.12a: *Iron Garnets*, Springer, Berlin 1977.
- [13] A.Maziewski, K.Mroczek, A.Stankiewicz, M.Tekielak and M.Kisielewski, Advances in Magneto-Optics II (Proc. 2nd Int.Symp. Magneto-Optics), Fiz.Nizk.Temp., 18 (S1), 377 (1992).
- [14] A.Maziewski and A.Stankiewicz, Proc. of SPIE, 859, 206 (1987).
- [15] A.Maziewski, A.Stankiewicz, M.Tekielak and V.V.Volkov, Advances in Magneto-Optics II (Proc. 2nd Int.Symp. Magneto-Optics), Fiz.Nizk.Temp., 18 (S1), 371 (1992).
- [16] R.Gieniusz and A.Maziewski, Sci. mat. Warsaw Univ. Branch Bialystok, 25, 77 (1980).

- [17] J.S.Brzosko (private communication).
- [18] A.Maziewski, First quarterly progress report on the Special Project SPC-93-4022.
- [19] E.Kubajewska, A.Maziewski and A.Stankiewicz, Thin Solid Films, 175, 299 (1989).

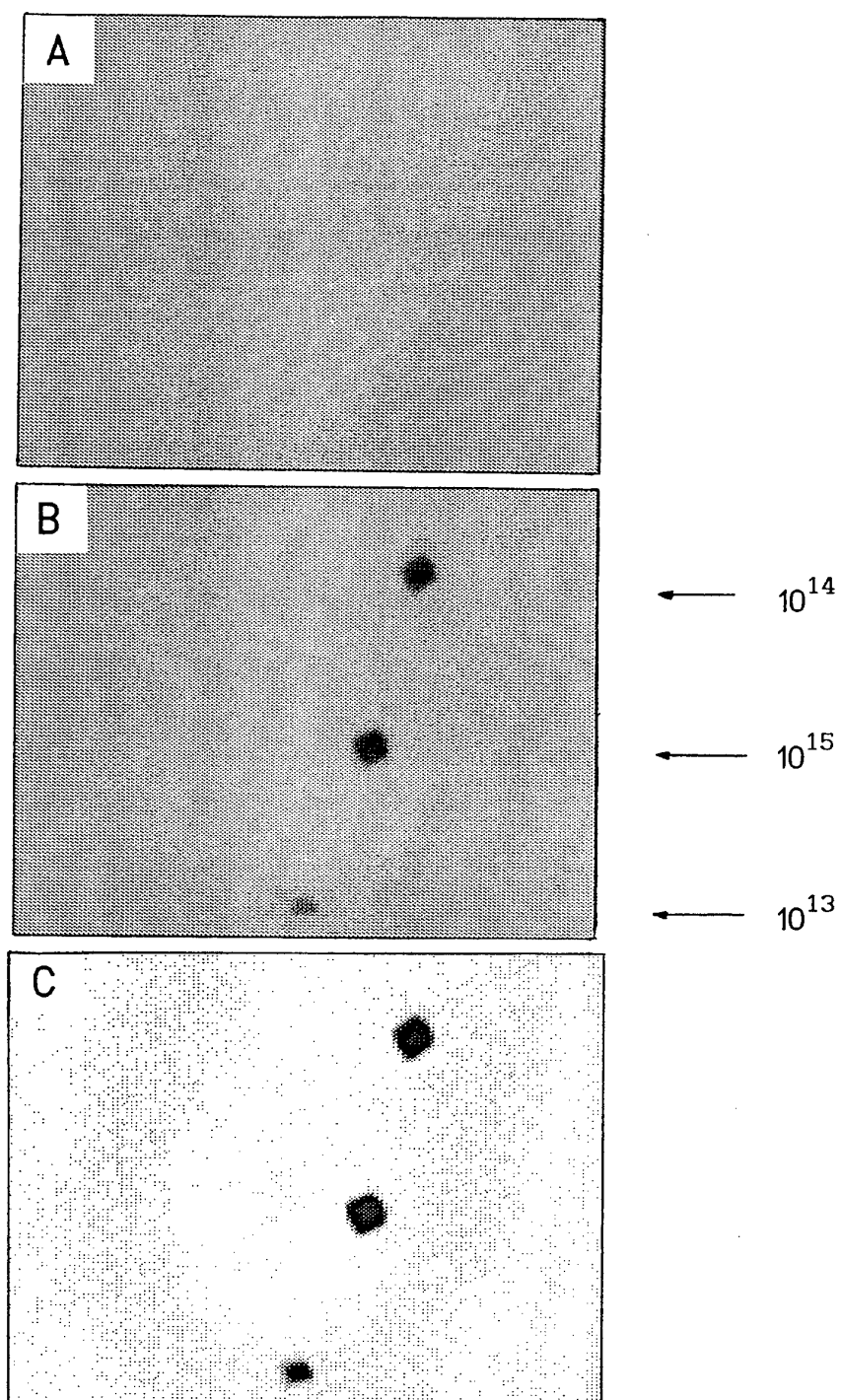


Figure 1: General picture of film 1 surface before (A) and after (B) implantation. Correlation image (C) presents differences between A and B.

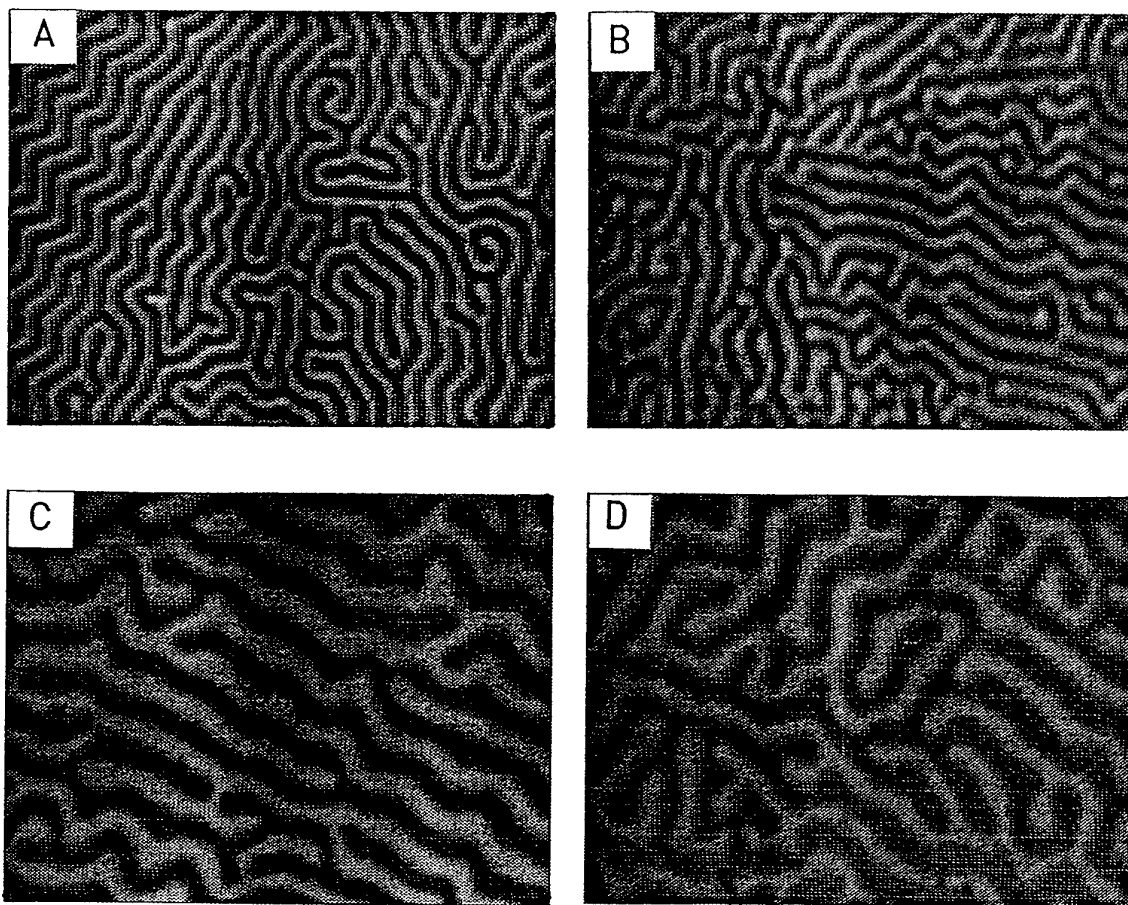


Figure 2: Domain structure of film 1 after demagnetization: before implantation (A), after D^+ -implantation with doses 10^{13} (B), 10^{14} (C), 10^{15} (D).

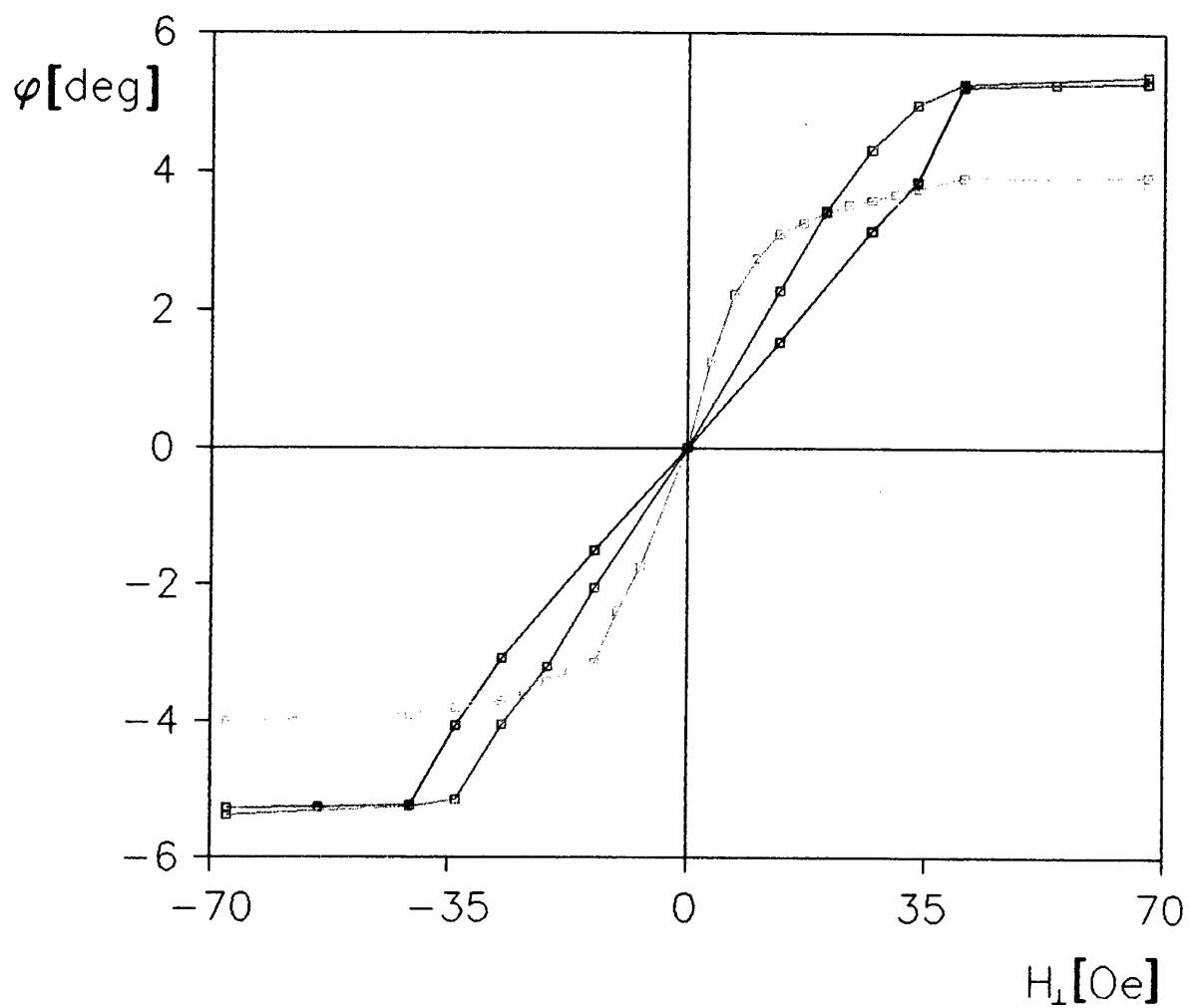


Figure 3: Faraday rotation φ vs. perpendicular magnetic field H_{\perp} for sample 1: before implantation (blue), after D^+ -implantation with doses 10^{13} (red), 10^{14} (green), 10^{15} (yellow).

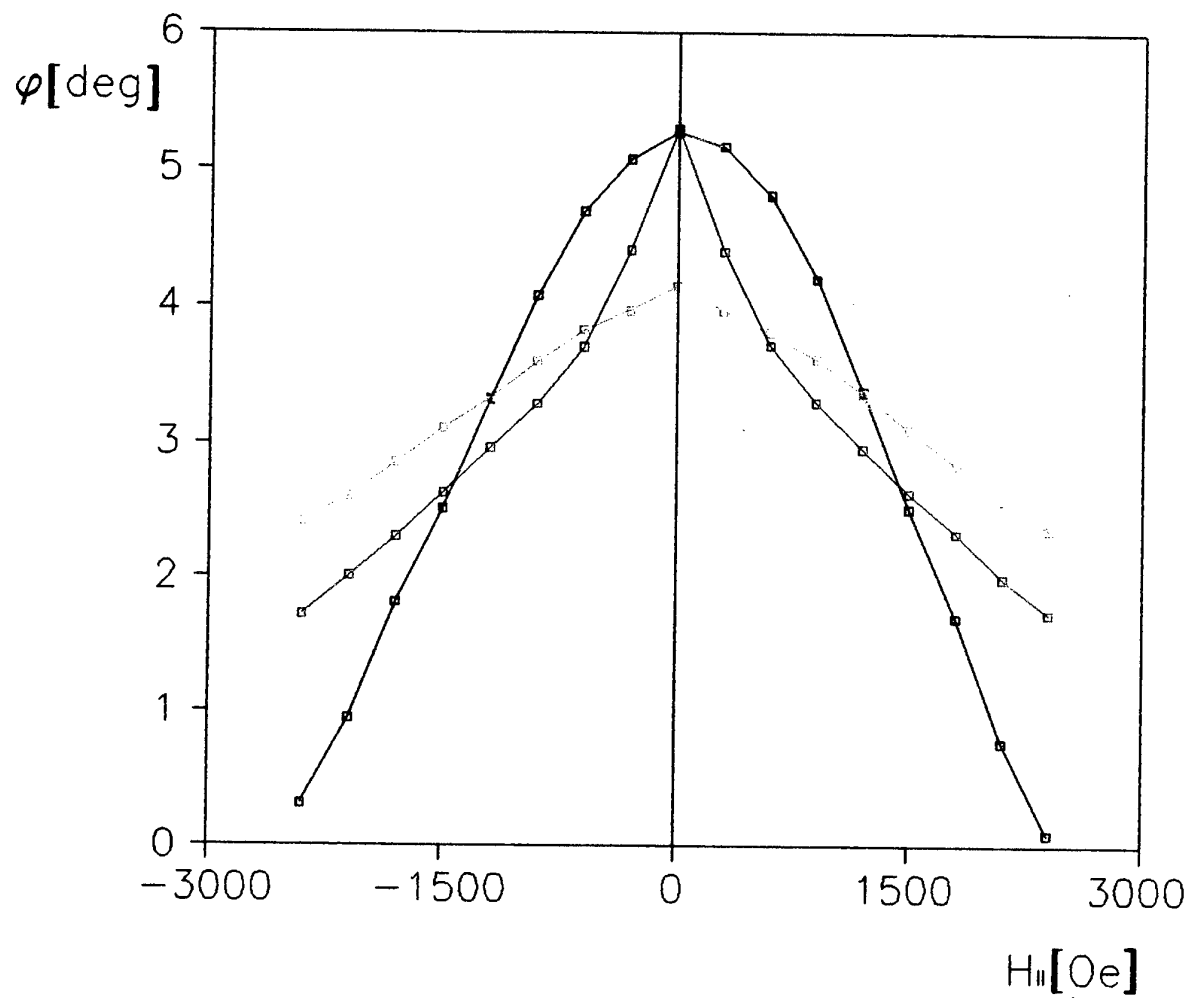


Figure 4: Faraday rotation φ vs. in-plane magnetic field $H_{||}$ for sample 1: before implantation (blue), after D^+ -implantation with doses 10^{13} (red), 10^{14} (green), 10^{15} (yellow). The constant bias field $H_{\perp} = 70\text{Oe}$ were kept during measurement.

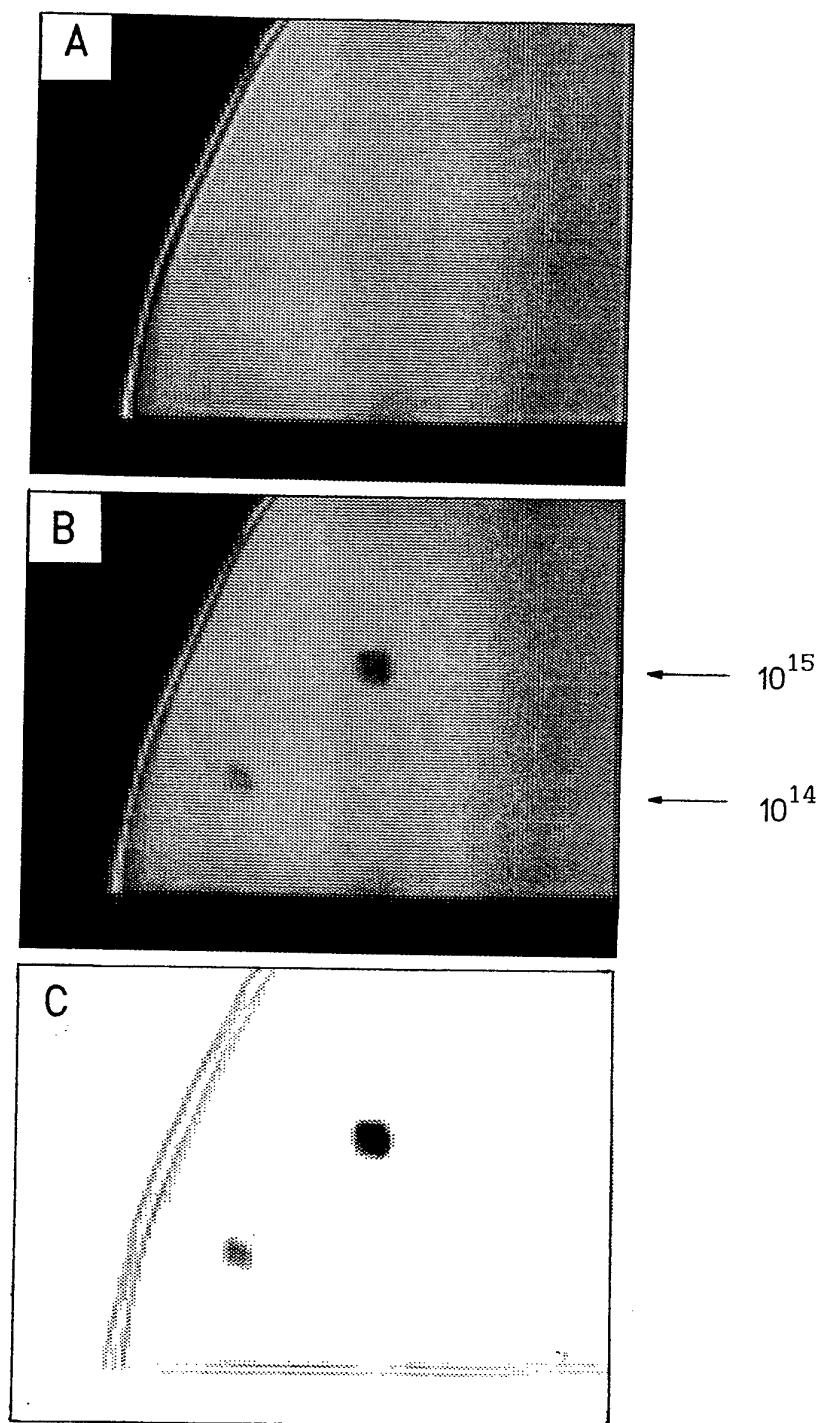


Figure 5: General picture of film 2 surface before (A) and after (B) implantation. Correlation image (C) presents differences between A and B.

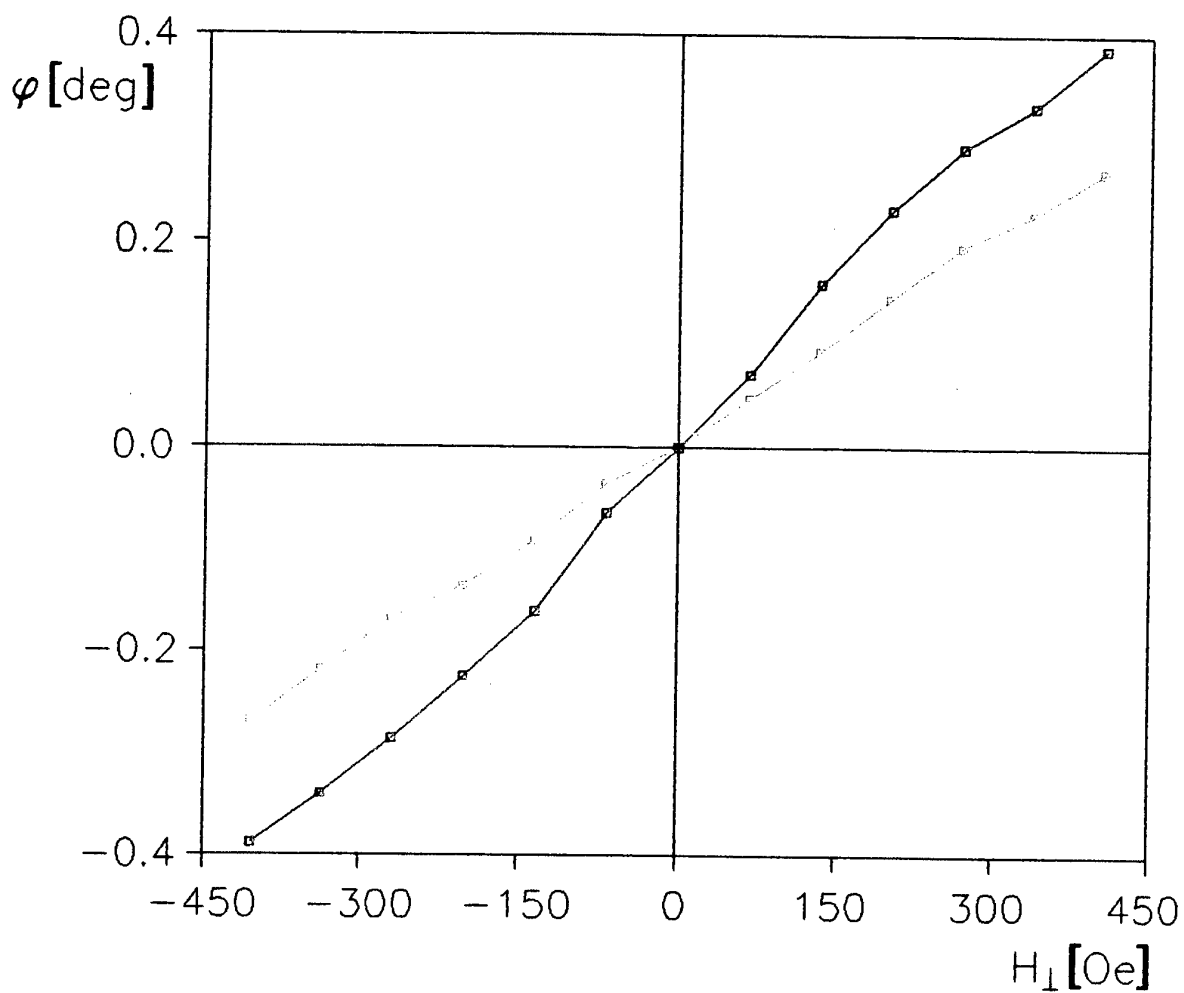


Figure 6: Faraday rotation φ vs. perpendicular magnetic field H_{\perp} for sample 2: before implantation (blue), after D^{+} -implantation with doses 10^{14} (green), 10^{15} (yellow).

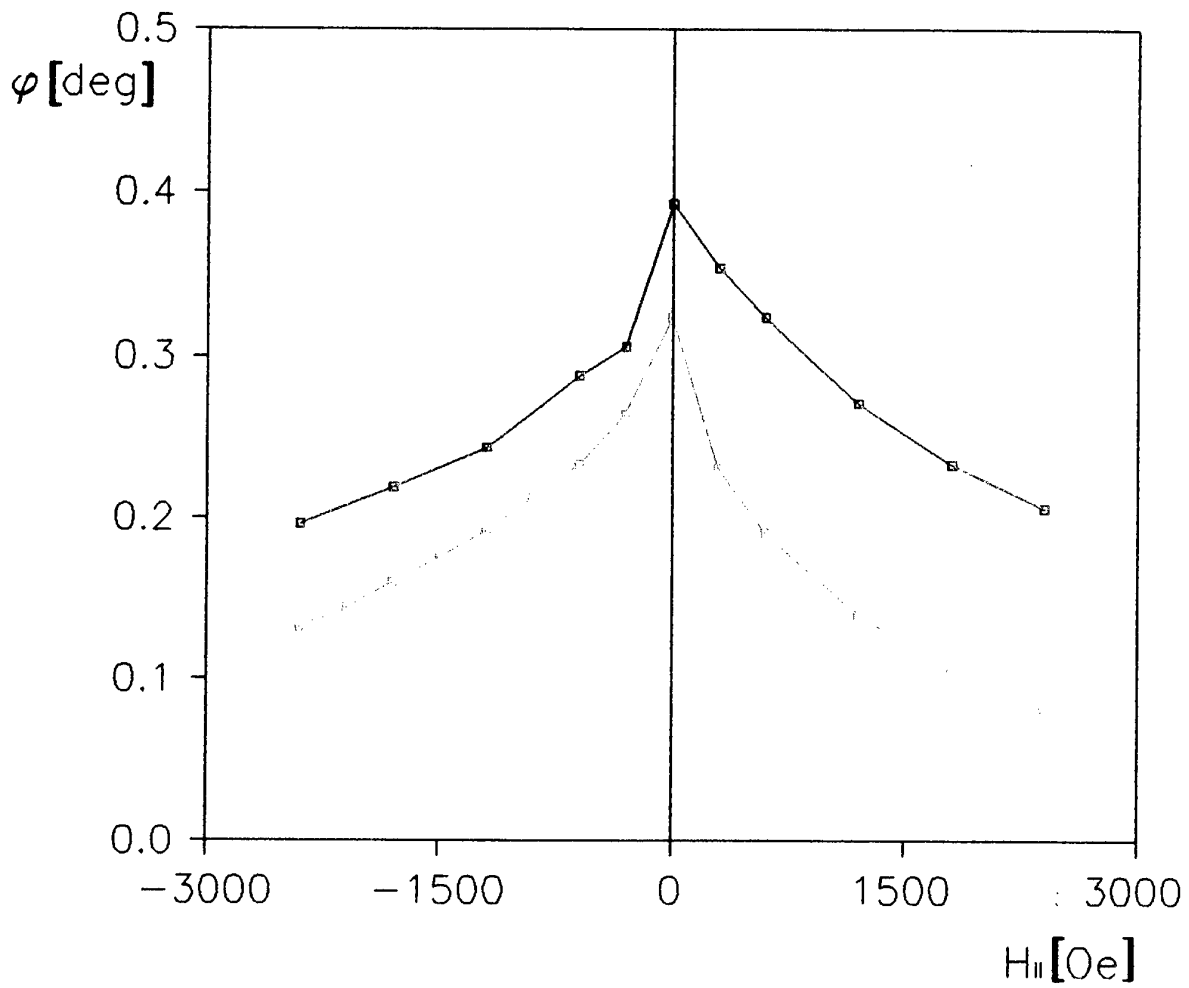


Figure 7: Faraday rotation φ vs. in-plane magnetic field $H_{||}$ for sample 2: before implantation (blue), after D^+ -implantation with doses 10^{14} (green), 10^{15} (yellow). The constant bias field $H_{\perp} = 400\text{Oe}$ were kept during measurement.

DETECTION OF PLASMA CLUSTERS WITH THIN MAGNETIC FILMS

Technical Feasibility Study

Third quarterly progress report
Special Project No. SPC-93-4022

Andrzej Maziewski
Warsaw University Branch
41 Lipowa Street
15-424 Bialystok
POLAND

2 February 1994

Abstract

The third quarterly progress report presents a continuation of the simulations of a plasma cluster impacts on magnetic garnet thin film surface. Just like before, the deuterium beam was used as the stimulating agent, but now the range of particle energy in the beam was extended up to two values: 0.5 and 1.6 MeV. The range of dose was also extended and the following doses were used: 10^{13} , 10^{14} , 10^{15} and $3 \cdot 10^{15}$ ions/mm². Two samples of YIG:Bi with different initial magnetic properties were processed. A new technique of illustration of implanted areas based on Faraday effect was developed. Areas implanted with dose higher than 10^{14} were easy visible using this technique. Implanted areas were also visible due to stress induced optical birefringence for some studied spaces. The analysis of magnetic properties of the implanted regions was also done using a magneto-optical magnetometer. It was found, that measured samples were sensitive to the applied implantation energies and doses, showing strong changes of their initial magnetic properties, especially for the two highest doses.

1 EXPERIMENT

Investigations were carried out on thin films of bismuth-doped yttrium iron garnet (YIG:Bi). The 3-in-diameter samples were grown by standard liquid phase epitaxy method on [111]-oriented gadolinium gallium garnet (GGG) substratum. The two samples chosen for the investigation had different initial magnetic properties: **Film 1** had large uniaxial anisotropy perpendicular to the plane of the sample, **Film 2** had anisotropy of easy plane type. These samples were implanted by deuterium ions beam providing two following values of implantation energy: 0.5 and 1.6 MeV, and four following values of implantation dose: 10^{13} , 10^{14} , 10^{15} and $3 \cdot 10^{15}$ ions/mm². For stabilization of the implantation conditions (by discharging the sample during the implantation), the samples were covered before the implantation by an uniform, 0.1 μ m thick, aluminium layer. The shape of the implanted areas was approximately rectangular with the linear dimension about 1 mm.

Because of the absorption changes for the light transmitted through the sample, the implanted areas were easily visible (excluding the case of the lowest dose). This effect was used as a method for visualization of implanted regions, see our previous report [1]. Absorption changes could be connected with specificity of our implantation. So it was important to develop a method of illustration of the implanted areas, based on magnetic properties changes of the used magnetic films. The method, actually discussed is based on the magneto-optical properties of the sample. Putting the sample into a specially adapted optical polarizing microscope, made it possible to find out the spatial distribution of Faraday rotation both in the implanted region and in its neighbourhood. The adaptation of polarizing microscope, which have been used before as a part of digital image processing set-up in thin magnetic films investigation [1], was based on lowering the optical magnification of it down to about 1. The images obtained in the microscope were registered by CCD camera and digitized by a frame grabber connected to IBM PC. In order to both increase the contrast of images and to compensate the heterogeneity of illumination, a special image modulation technique [2] was used. The most powerful and quick-acting version of it was based on image registration for two different angles between polarizer

and analyzer, namely $+\alpha$ and $-\alpha$ ($\alpha=0$ means exactly crossed position of polarizer and analyzer). Faraday rotation φ of each point of the image, described by spatial coordinates (m,n) , could be calculated in this case using the following formula (valid on condition that: 1) α and φ are small enough to fulfil the $\sin(x) \approx x$ -type approximation, 2) $\alpha > \varphi$):

$$\varphi(m,n) = \alpha * [(I_1(m,n))^{1/2} - (I_2(m,n))^{1/2}] / [(I_1(m,n))^{1/2} + (I_2(m,n))^{1/2}]$$

where $I_1(m,n)$ and $I_2(m,n)$ are the intensities of the light in the (m,n) point of two images registered for $+\alpha$ and $-\alpha$, respectively. The $\varphi(m,n)$ values, obtained after such procedure, was expressed on the final image in terms of light intensity levels. $\varphi(m,n)$ images were represented - for convenience - in coloured graduation, see Figs. 1-11.

Images of the Faraday rotation spatial distribution obtained for different values of the magnetic field H_{\perp} perpendicular to the plane of the sample 1 for implantation regions are shown on Figs 1-6. Figs 1a, 2a, 3a, 4a, 5a, and 6a represent the demagnetized state of the sample. The demagnetization had been done using the sinusoidally changeable magnetic field H_{\perp} with decreasing amplitude. Although domain structure existed in non-implanted areas in the demagnetized state, it could not be visible on the above-mentioned figures because of too small domain period ($\approx 30\mu m$) in relation to the resolution of the optical set-up. After applying magnetic field H_{\perp} with amplitude insufficient to sample saturation, a part of domain disappeared, the domain structure period became larger and the remained domain was visible - as one could see on Figs 1b, 2b, 3b, 4b, 5b and 6b. In the case of sample 1, the implantations with dose 10^{13} and both energies did no produce any optically and magnetooptically observable effects.

Similar images of sample 2 obtained for different values of magnetic field H_{\perp} for implantation with the energy 1.6 MeV and doses $3 \cdot 10^{15}$, 10^{15} and the energy 0.5 MeV and doses $3 \cdot 10^{15}$, 10^{15} and 10^{14} are shown on Figs 7-11. The period of domain structure of sample 2 was so small ($\approx 3.8 \mu m$), that it was completely impossible to observe the domain structure in the used optical system in any magnetic field. The areas of implantation with the energy 1.6 MeV and doses 10^{14} and 10^{13} , and the energy 0.5 MeV and dose 10^{13} , were fully undistinguishable using described methods.

An analysis of magnetic properties of the implanted regions was

done using computer-controlled magnetooptical magnetometer [3] working in Faraday's configuration with He-Ne laser as a source of light and a special Faraday rotation compensation system. The magnetometer gave the opportunity to measure the Faraday rotation dependence on H_{\perp} magnetic field.

Dependence of Faraday rotation on magnetic field H_{\perp} measured for sample 1 at non-implanted, and implanted with energy 1.6 MeV and doses 10^{14} , 10^{15} and $3 \cdot 10^{15}$ areas, is shown on Fig.12a,b. While on the Fig.12a one could see detail of this dependence in small range (± 150 Oe) of magnetic field, on Fig.12b one could see analogous curves obtained in wider range (± 1.5 kOe) of H_{\perp} . Similar dependence measured for areas implanted with energy 0.5 MeV and doses 10^{14} , 10^{15} and $3 \cdot 10^{15}$ is shown on Fig.13a,b.

Linear dependence of Faraday rotation on magnetic field H_{\perp} amplitude have been found out in the case of sample 2. It is drawn on Fig.14 for implantation energy 1.6 MeV and doses 10^{15} , $3 \cdot 10^{15}$, and on Fig.15 for the energy 0.5 MeV and doses 10^{14} , 10^{15} and $3 \cdot 10^{15}$. For comparison, the curve measured for non-implanted area, is also shown on both these figures.

2 DISCUSSION

Faraday rotation (measured at non-zero magnetic field) decreases with increasing ion implantation dose, see Figs. 12-15. This effect was used for visualization of implanted regions - as one could see in Figs. 1, 4, 5, 9, 10. The decrease of Faraday rotation could be connected with the increasing of in-plane anisotropy - an effect usually observed in implanted films and caused by an in-plane stress induced during implantation - see [1] and references therein. Such stresses also produce a optical birefringence. Characteristic optical birefringence-origin patterns around implanted areas, could be really seen in Fig.1, 2, 7, 8 and - in more weaker form - in Fig.9 and 10. This is a distinct confirmation of the existence of strong, non-uniform stress around the region implanted with particles of higher energy.

In the case of sample 1, one could observe a strong influence of implantation on such parameters of domain structure, as for example period of domain structure (see Fig.4 and 5) and saturation magnetic

field (see Fig.12a and 13a).

One could notice some special features of magnetic effects produced by the higher energy of implantation and the lower one:

1.6 MeV:

1) Demagnetized state, sample 1 (Figs.1a, 2a, 3a) - domain structure is not visible in the used optical resolution; because of difference in domain structure in unimplanted and implanted ($3 \cdot 10^{15}$ dose) regions one can distinguish them, see Fig.1a.

2) Hysteresis loops, sample 1 (Fig.12) - only for $3 \cdot 10^{15}$ dose implanted region there is drastic difference in magnetization curve comparison with non-implanted one,

3) Hysteresis loops, sample 2 (Fig.14) there is small difference in magnetization curves obtained for different doses; similarity of all curves,

0.5 MeV:

1) Demagnetized state, sample 1 (Figs 4a and 5a) - the existence of domain structure with large period in comparison with one in unimplanted region,

2) Hysteresis loops, sample 1 (Fig.13) - influence of implantation on magnetization curve is visible starting from 10^{14} dose; increasing the dose one can find a kind of saturation of that influence;

3) Hysteresis loops, sample 2 (Fig.15) - there is small difference in magnetization curves obtained for different doses; this difference is greater than one in Fig.14.

These above discussed properties one could try to explain taking into consideration dependence of irradiation defects profile (defined by such parameters as e.g. maximum of defects density and the maximum spatial position l_{imax} measured from the sample surface, parameters describing shape of the profile) on implantation energy and dose. For example the increase of l_{imax} parameter was reported [4] increasing implantation ion energy. Ion dose influence on damages profile shape was studied in the papers [5,6]. In a case of the relatively low implantation dose : the face layer of implanted film is not so strongly damaged, damages profile is relatively narrow. For high dose - the profile of implantation becomes broad and flat near the face surface.

One could expect, that for our samples, in the case of the higher implantation energy (which is really extremely high in comparison with usually applied and reported in the literature values) the l_{imax} value is greater than the magnetic layer thickness. This could be the reason that for the discussed higher energy case it is necessary to use higher (in comparison with the case of lower energy) implantation doses to obtain visible changes of magnetic properties.

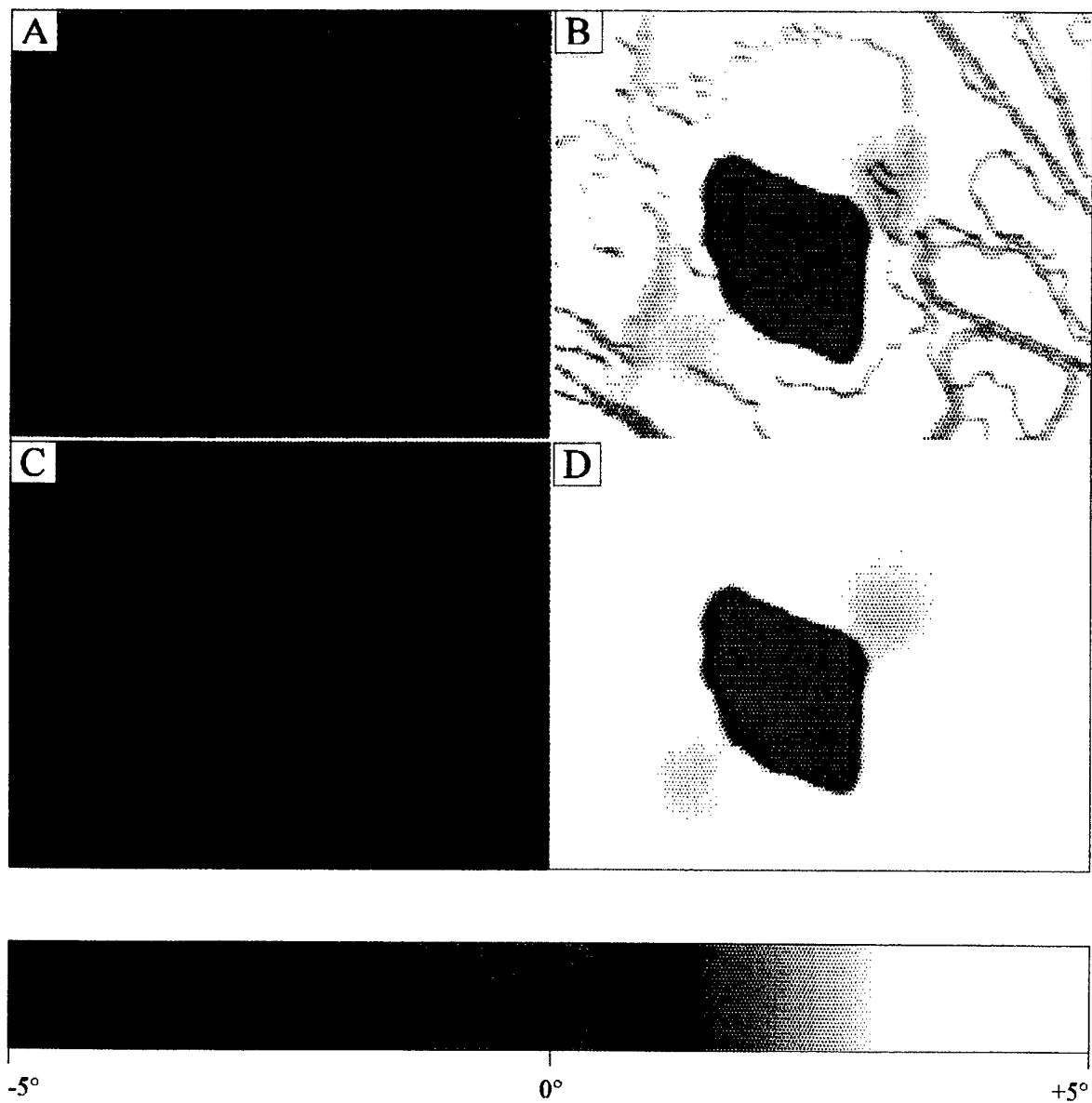
3 CONCLUSIONS

The proposed method, based on Faraday effect, seems to be powerful technique for visualization of implantation region. One can use also the other method of visualization based on optical birefringence induced by stress caused by implantation. This second method could be interesting for : (i) magnetic film with in-plane magnetization (our sample 2); (ii) nonmagnetic films.

Used implantation conditions were chosen similar to those, which one can expect during plasma focus irradiation. It was found, that measured samples were sensitive to both applied implantation energies and to the two highest doses, showing strong changes of their initial magnetic properties. From the experimental point of view, sample 1 seems to be more comfortable, showing greater dynamics of changes of measured parameters.

4 LITERATURE

- [1] A.Maziewski, First quarterly progress report on the Special Project No. SPC-93-4022.
- [2] A.Maziewski, K.Mroczek, A.Stankiewicz, M.Tekielak, M.Kisielewski, Advances in Magneto-Optics II, Proc. 2nd Int.Symp. Magneto-Optics, Fiz.Nizk.Temp., vol 18, Suppl. No.S1, 377 (1992).
- [3]. M.Marysko, A.Maziewski, A.Stankiewicz, M.Tekielak, V.V.Volkov, Magnetic anisotropy investigation in (210)-oriented Bi-substituted magnetic garnets, Physica B 190, 190 (1993).
- [4] H.A.Washburn, G.Galli, J.Appl.Phys., 50(3), 2287 (1979).
- [5] P.Gerard, Thin Solid Films, 114, 3 (1984).
- [6] C.H.Wilts, A.Urai, J.Appl.Phys., 64(9), 4632 (1988).



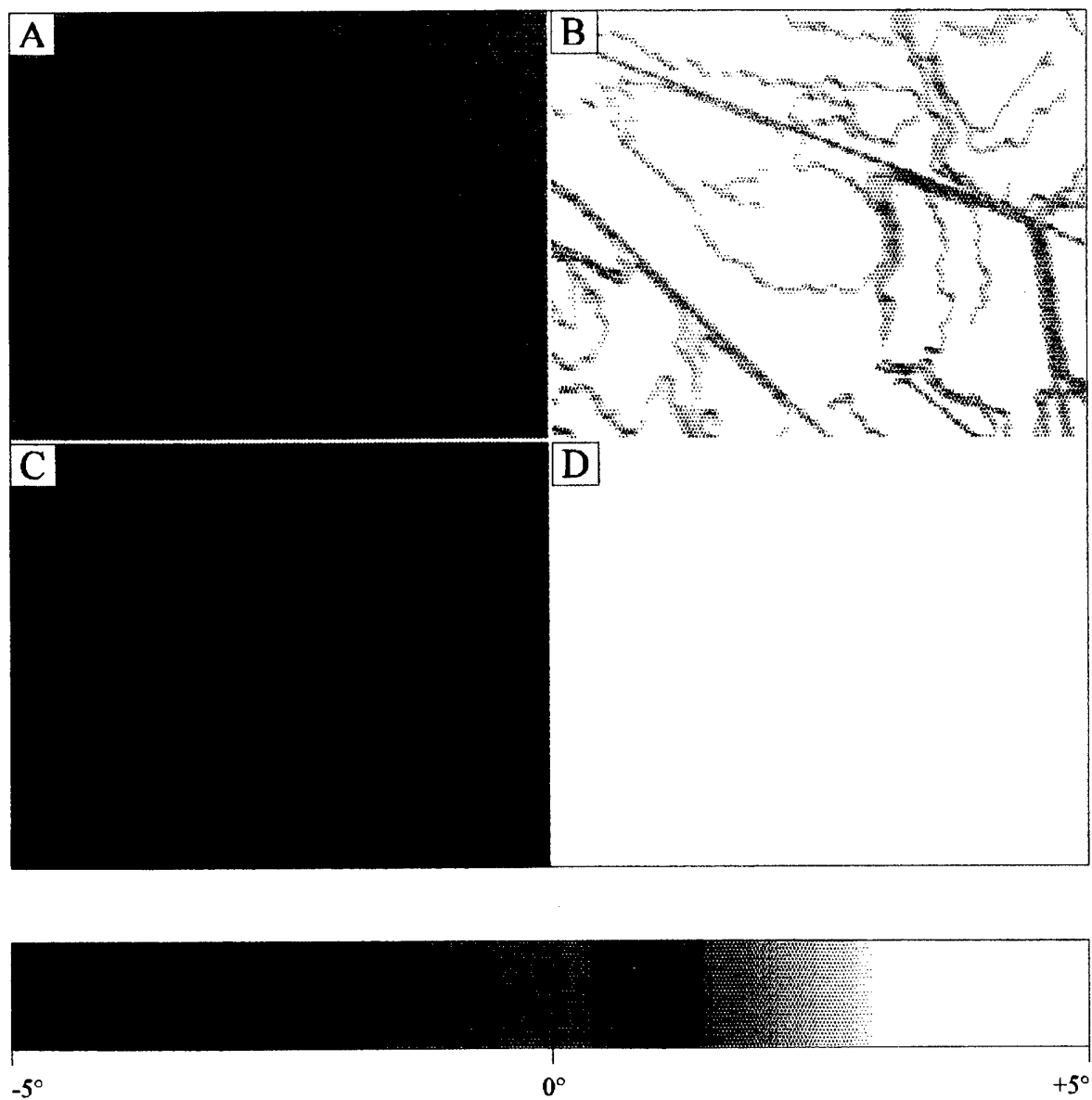


Figure 2 : Spatial distribution of Faraday rotation of the sample 1 obtained for the region of D^+ -implantation with the dose 10^{15} and the energy 1.6 MeV. Images were registered at different values of magnetic field H_{\perp} perpendicular to the plane of the sample:

- A) $H_{\perp} = 0$, (after demagnetization),
- B) $H_{\perp} = +40$ Oe,
- C) $H_{\perp} = -80$ Oe,
- D) $H_{\perp} = +80$ Oe.

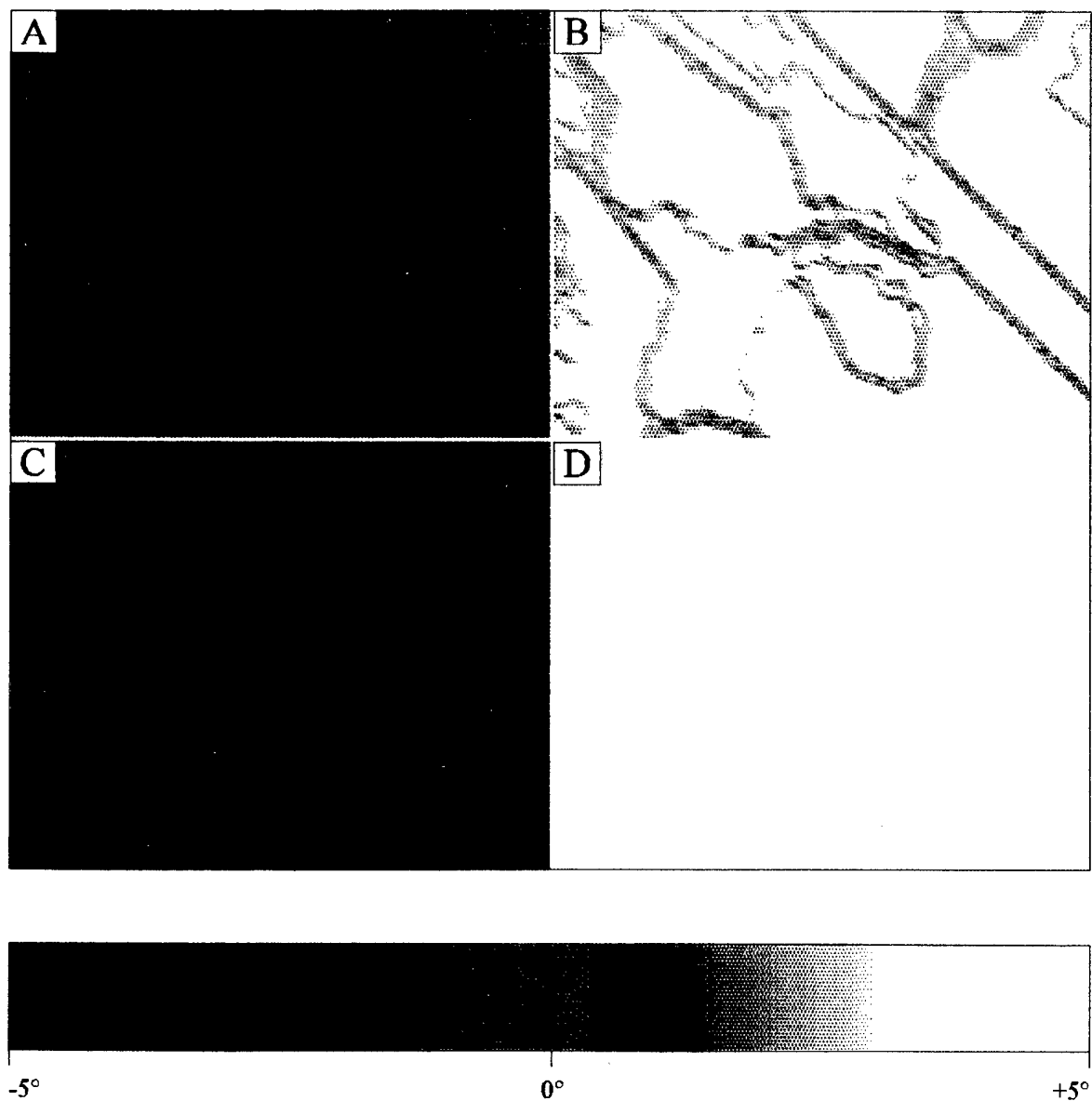
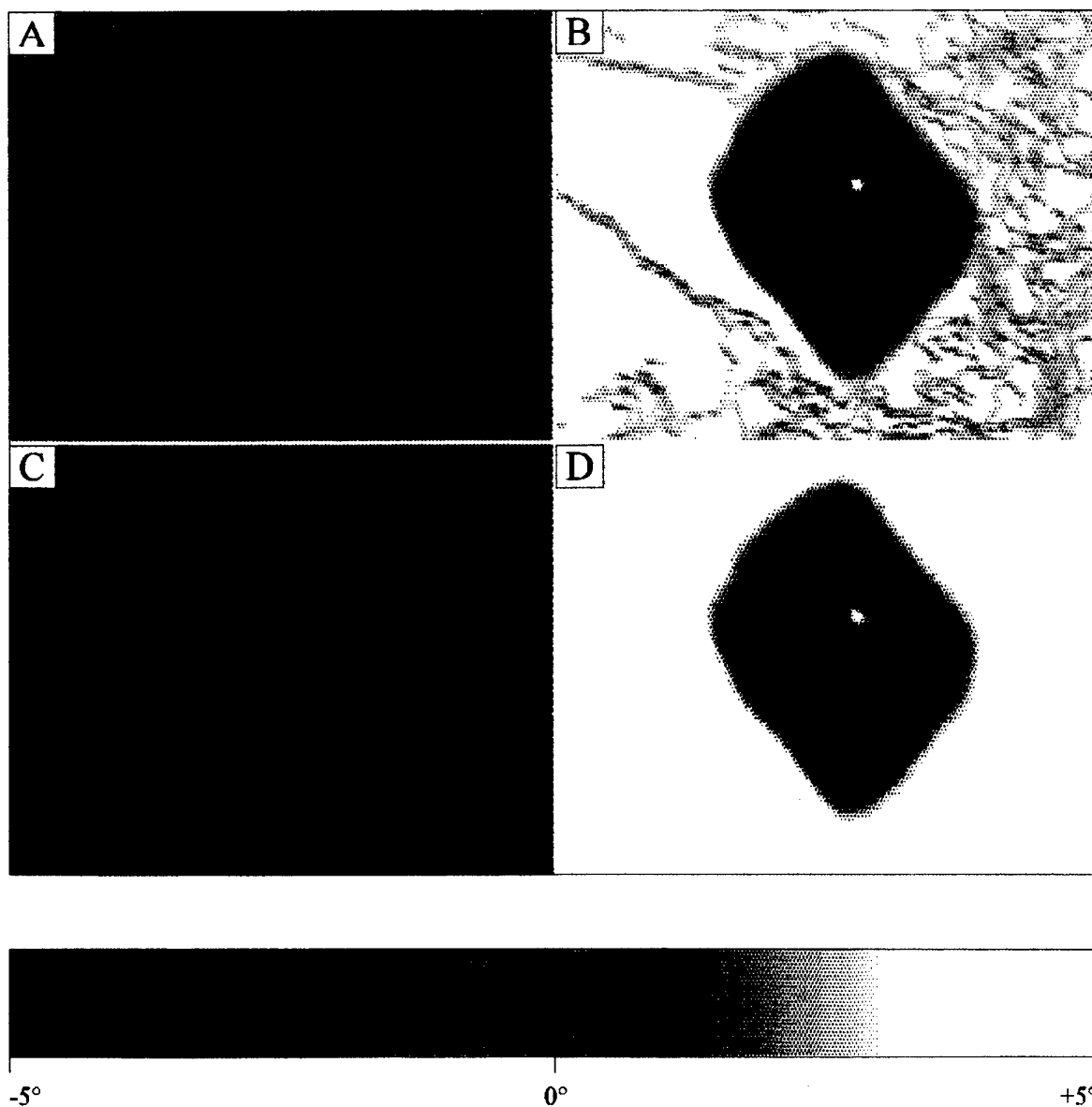


Figure 3 : Spatial distribution of Faraday rotation of the sample 1 obtained for the region of D^+ -implantation with the dose 10^{14} and the energy 1.6 MeV. Images were registered at different values of magnetic field H_{\perp} perpendicular to the plane of the sample:

- A) $H_{\perp} = 0$, (after demagnetization),
- B) $H_{\perp} = +40$ Oe,
- C) $H_{\perp} = -80$ Oe,
- D) $H_{\perp} = +80$ Oe.



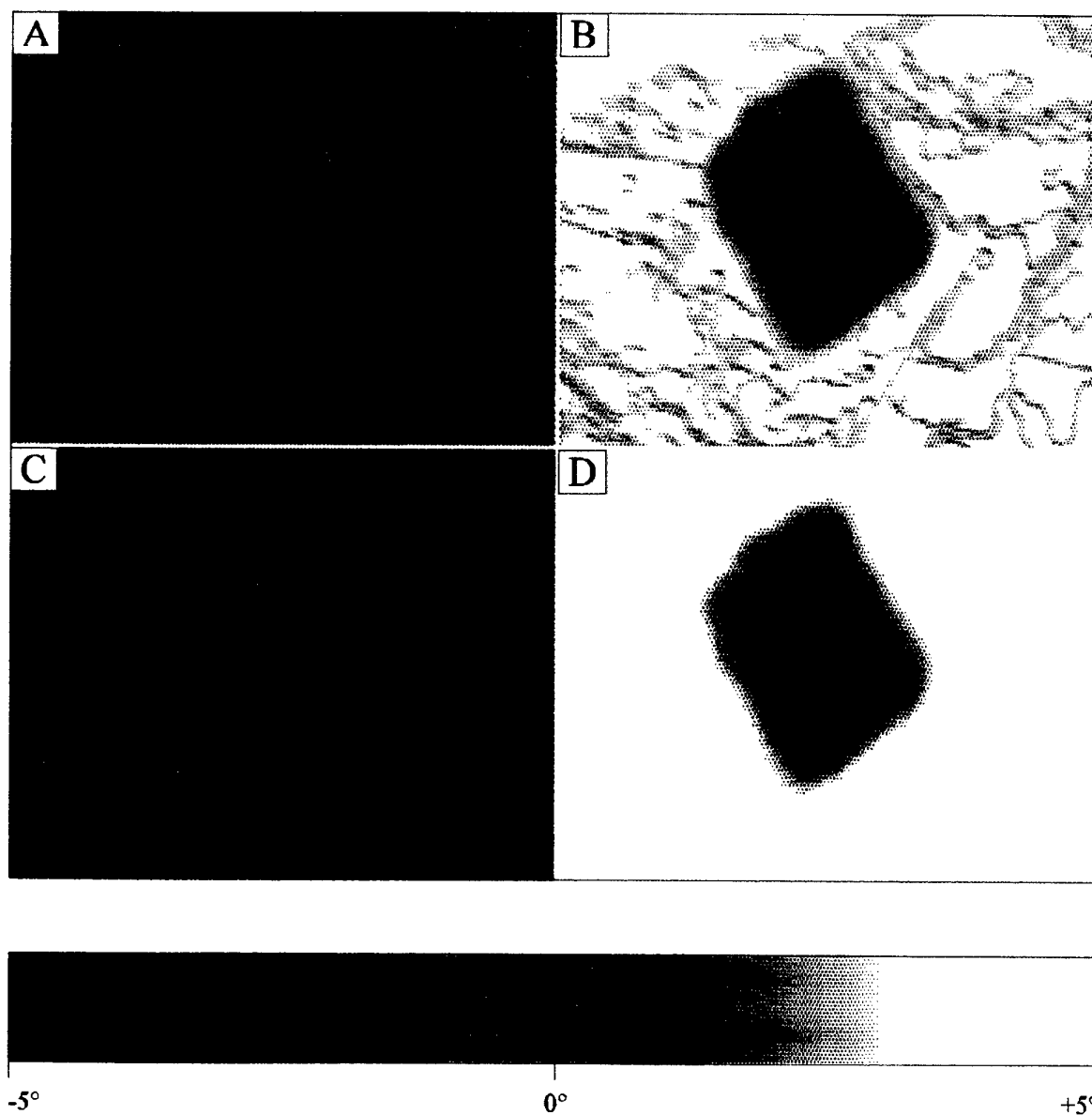


Figure 5 : Spatial distribution of Faraday rotation of the sample 1 obtained for the region of D^+ -implantation with the dose 10^{15} and the energy 0.5 MeV. Images were registered at different values of magnetic field H_{\perp} perpendicular to the plane of the sample:

- A) $H_{\perp} = 0$, (after demagnetization),
- B) $H_{\perp} = +40$ Oe,
- C) $H_{\perp} = -80$ Oe,
- D) $H_{\perp} = +80$ Oe.

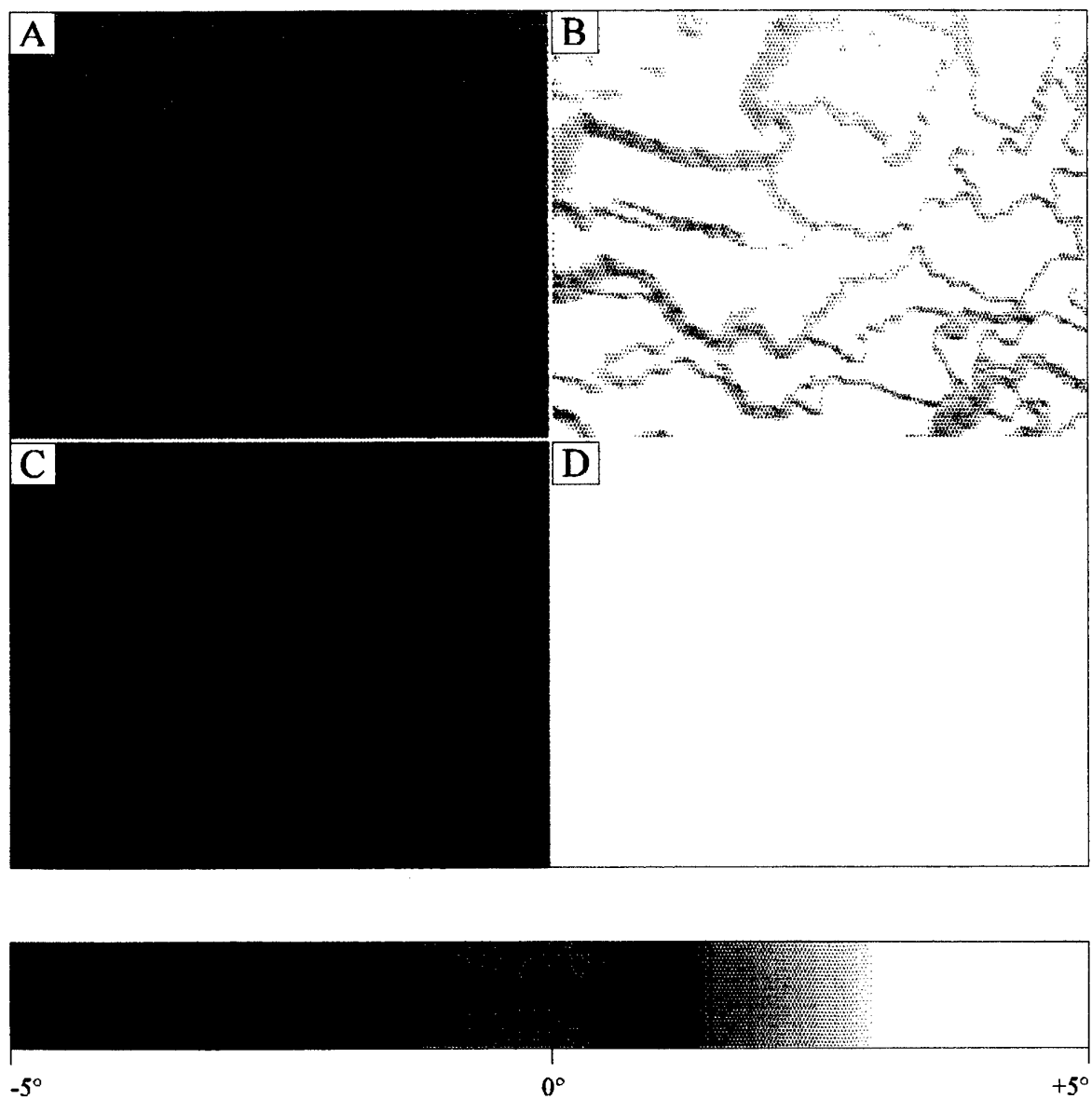


Figure 6 : Spatial distribution of Faraday rotation of the sample 1 obtained for the region of D^+ -implantation with the dose 10^{14} and the energy 0.5 MeV. Images were registered at different values of magnetic field H_{\perp} perpendicular to the plane of the sample:

- A) $H_{\perp} = 0$, (after demagnetization),
- B) $H_{\perp} = +40$ Oe,
- C) $H_{\perp} = -80$ Oe,
- D) $H_{\perp} = +80$ Oe.

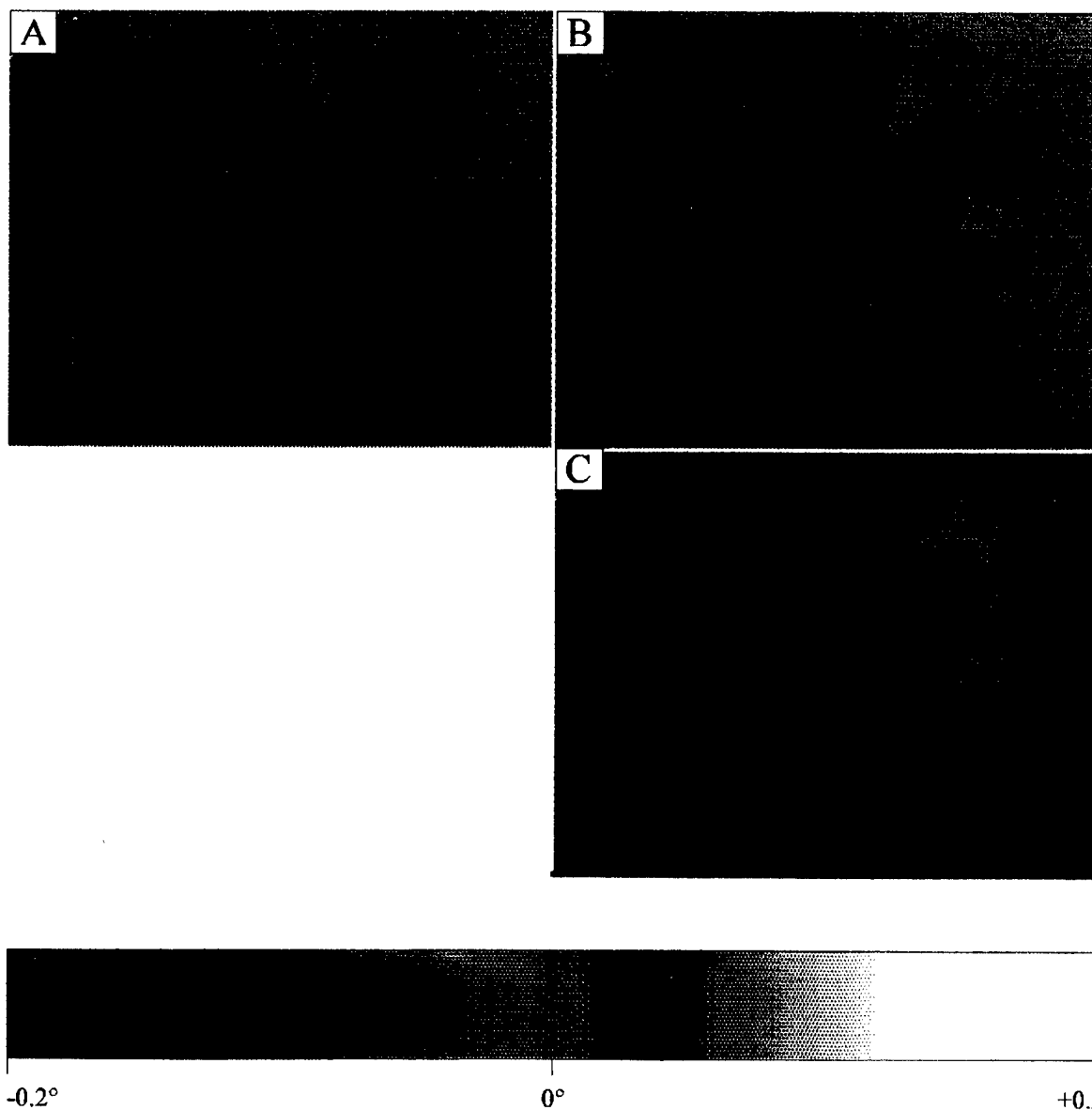


Figure 7 : Spatial distribution of Faraday rotation of the sample 2 obtained for the region of D^+ -implantation with the dose 3×10^{15} and the energy 1.6 MeV. Images were registered at different values of magnetic field H_{\perp} perpendicular to the plane of the sample:

- A) $H_{\perp} = 0$, (after demagnetization),
- B) $H_{\perp} = +450$ Oe,
- C) $H_{\perp} = -450$ Oe,

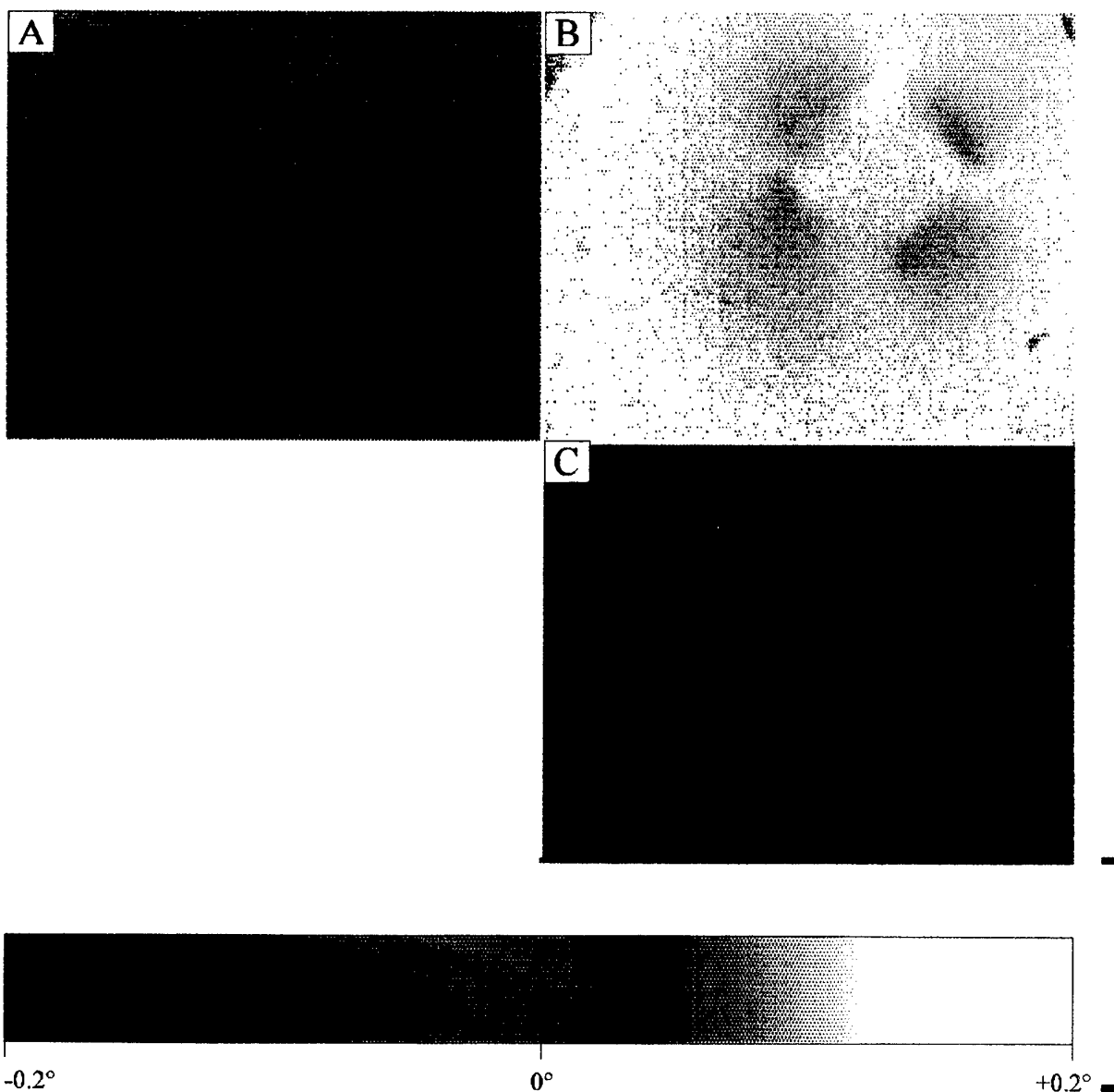


Figure 8 : Spatial distribution of Faraday rotation of the sample 2 obtained for the region of D^+ -implantation with the dose 10^{15} and the energy 1.6 MeV. Images were registered at different values of magnetic field H_{\perp} perpendicular to the plane of the sample:

- A) $H_{\perp} = 0$, (after demagnetization),
- B) $H_{\perp} = +450$ Oe,
- C) $H_{\perp} = -450$ Oe,

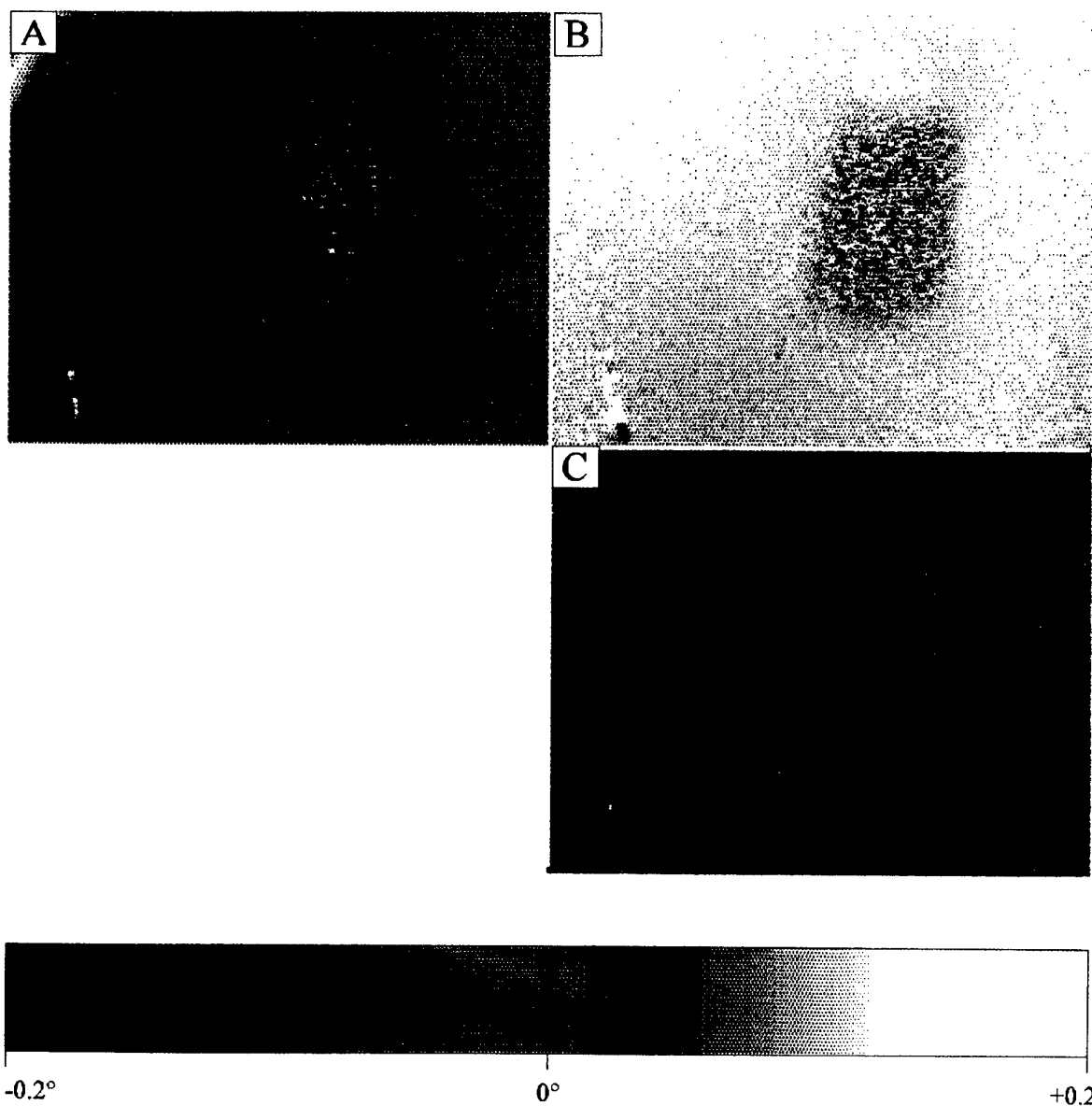


Figure 9 : Spatial distribution of Faraday rotation of the sample 2 obtained for the region of D^+ -implantation with the dose 3×10^{15} and the energy 0.5 MeV. Images were registered at different values of magnetic field H_\perp perpendicular to the plane of the sample:

- A) $H_\perp = 0$, (after demagnetization),
- B) $H_\perp = +450$ Oe,
- C) $H_\perp = -450$ Oe,

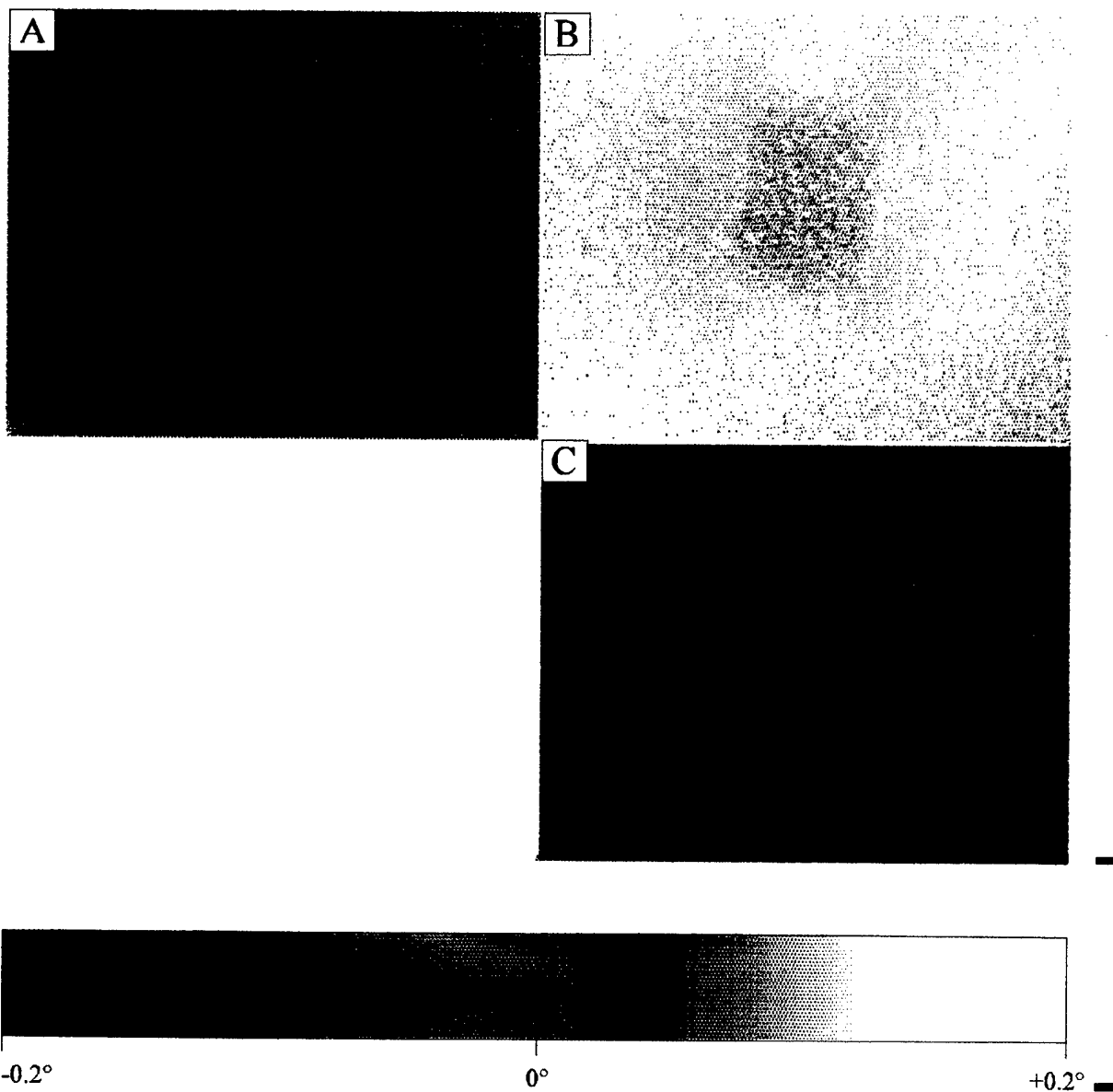


Figure 10 : Spatial distribution of Faraday rotation of the sample 2 obtained for the region of D^+ -implantation with the dose 10^{15} and the energy 0.5 MeV. Images were registered at different values of magnetic field H_{\perp} perpendicular to the plane of the sample:

- A) $H_{\perp} = 0$, (after demagnetization),
- B) $H_{\perp} = +450$ Oe,
- C) $H_{\perp} = -450$ Oe,

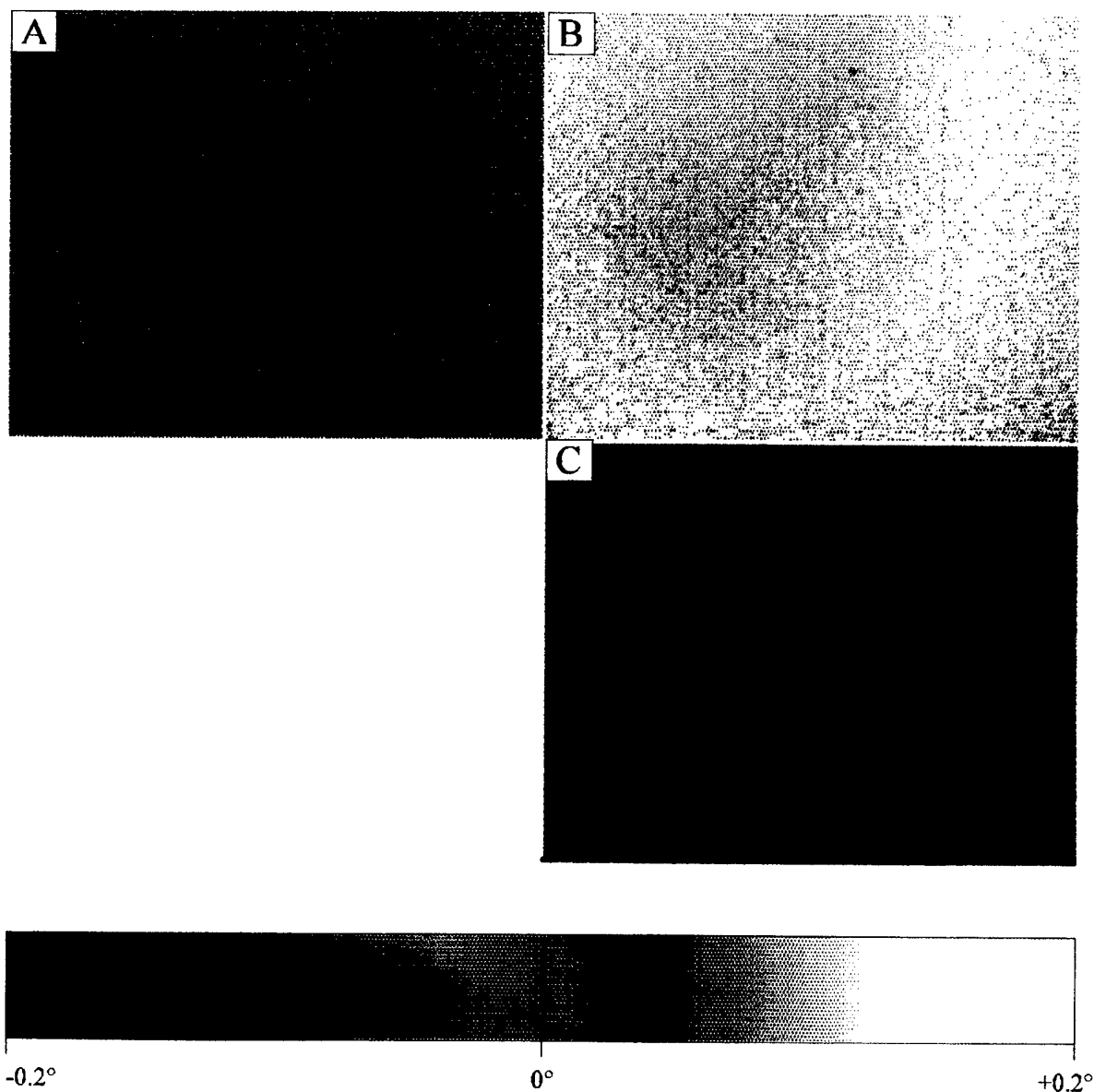
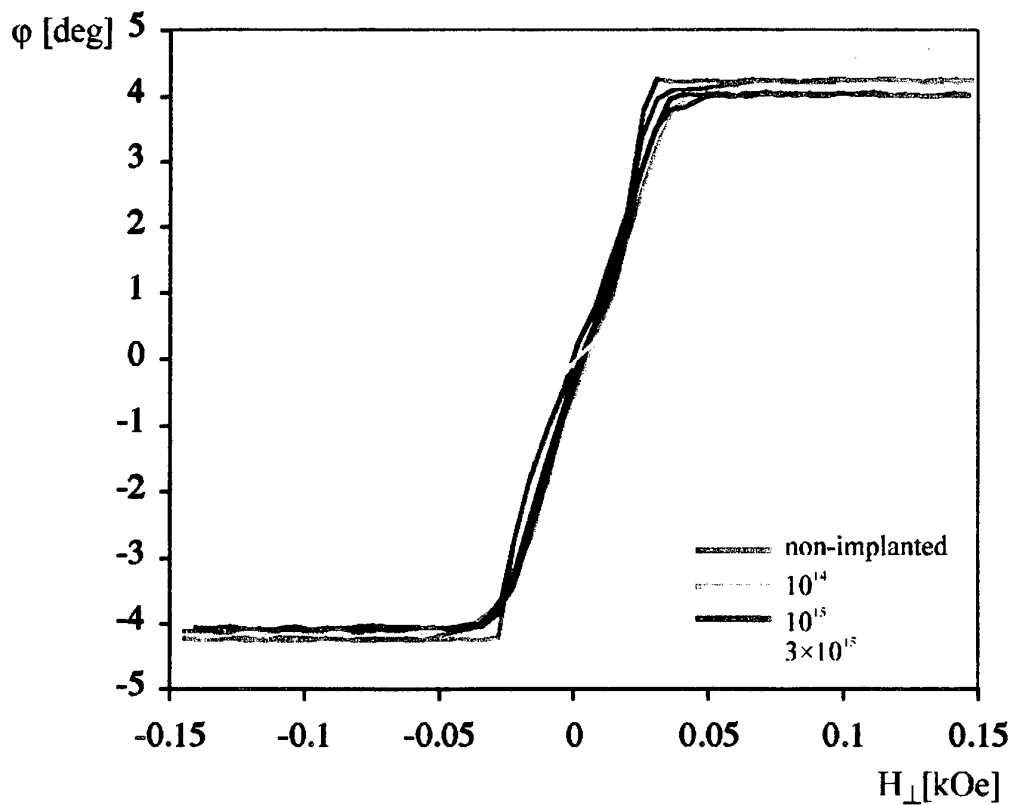


Figure 11 : Spatial distribution of Faraday rotation of the sample 2 obtained for the region of D^+ -implantation with the dose 10^{14} and the energy 0.5 MeV. Images were registered at different values of magnetic field H_{\perp} perpendicular to the plane of the sample:

- A) $H_{\perp} = 0$, (after demagnetization),
- B) $H_{\perp} = +450$ Oe,
- C) $H_{\perp} = -450$ Oe,

A)



B)

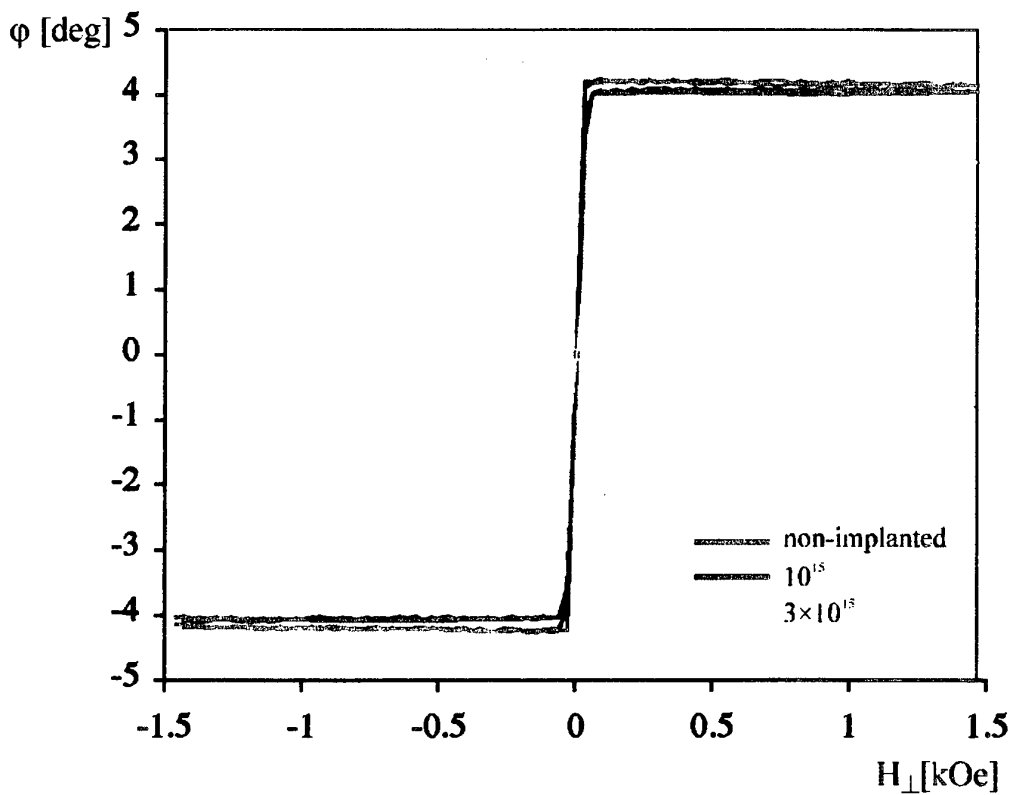
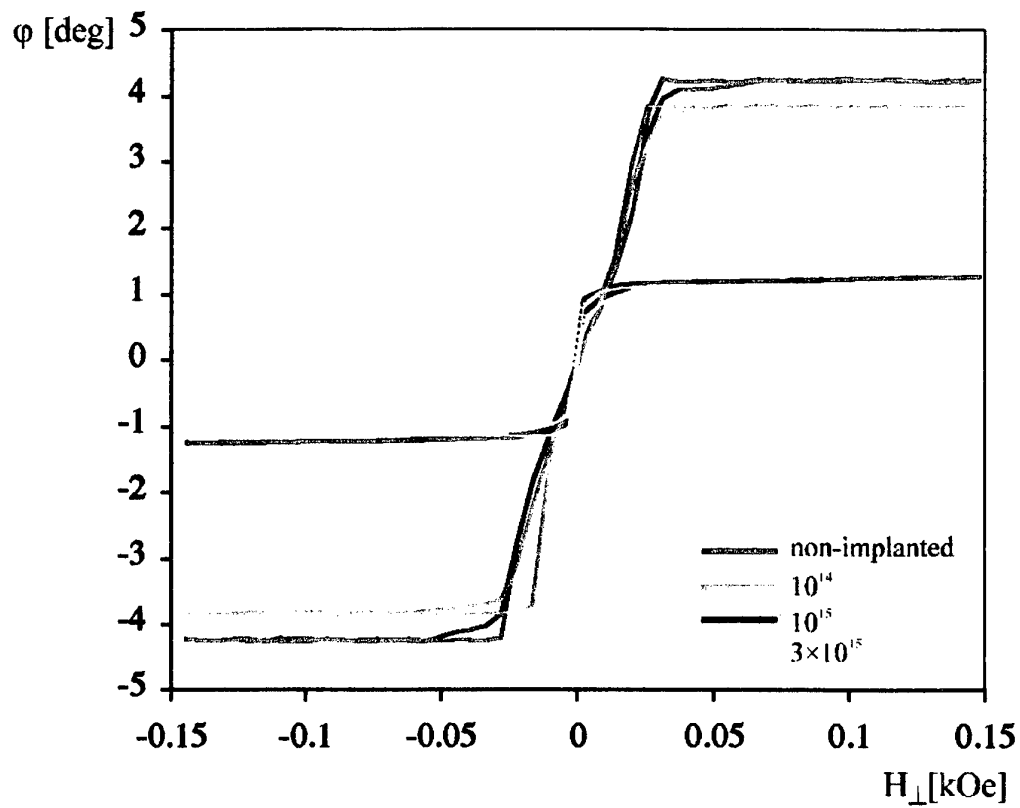


Figure 12 : Faraday rotation ϕ vs. magnetic field H_{\perp} measured for sample 1 at non-implanted area and D^+ -implanted areas with energy 1.6 MeV and different doses.

A)



B)

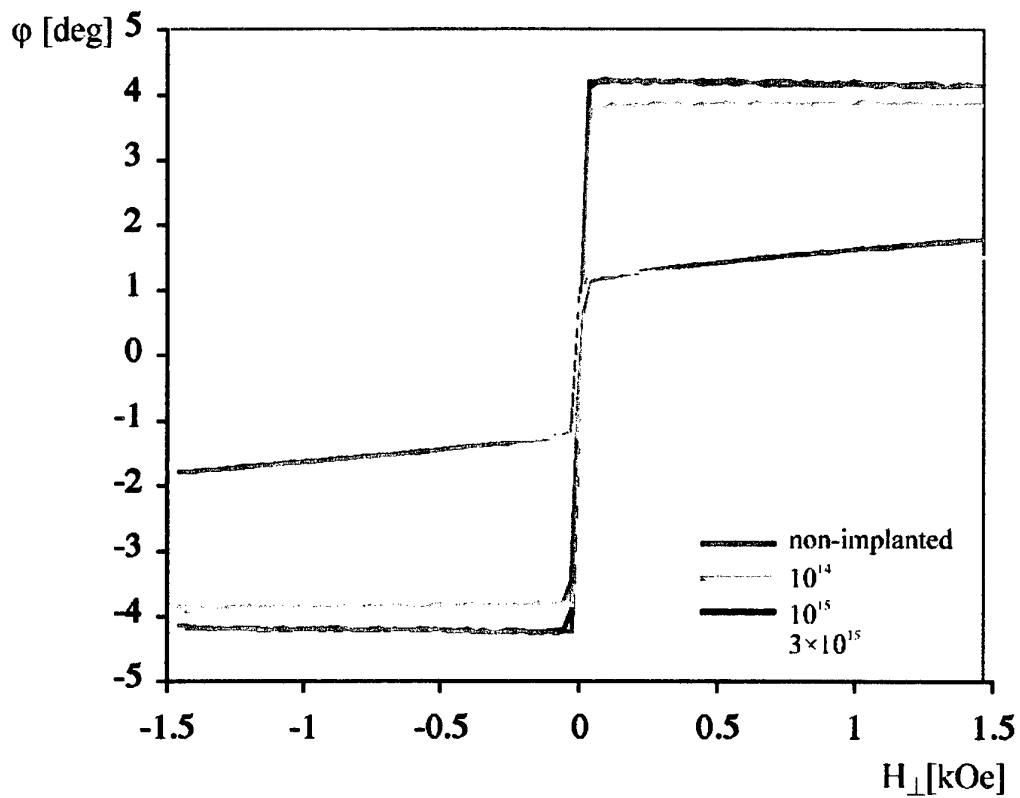


Figure 13 : Faraday rotation ϕ vs. magnetic field H_{\perp} measured for sample 1 at non-implanted area and D^+ -implanted areas with energy 0.5 MeV and different doses.

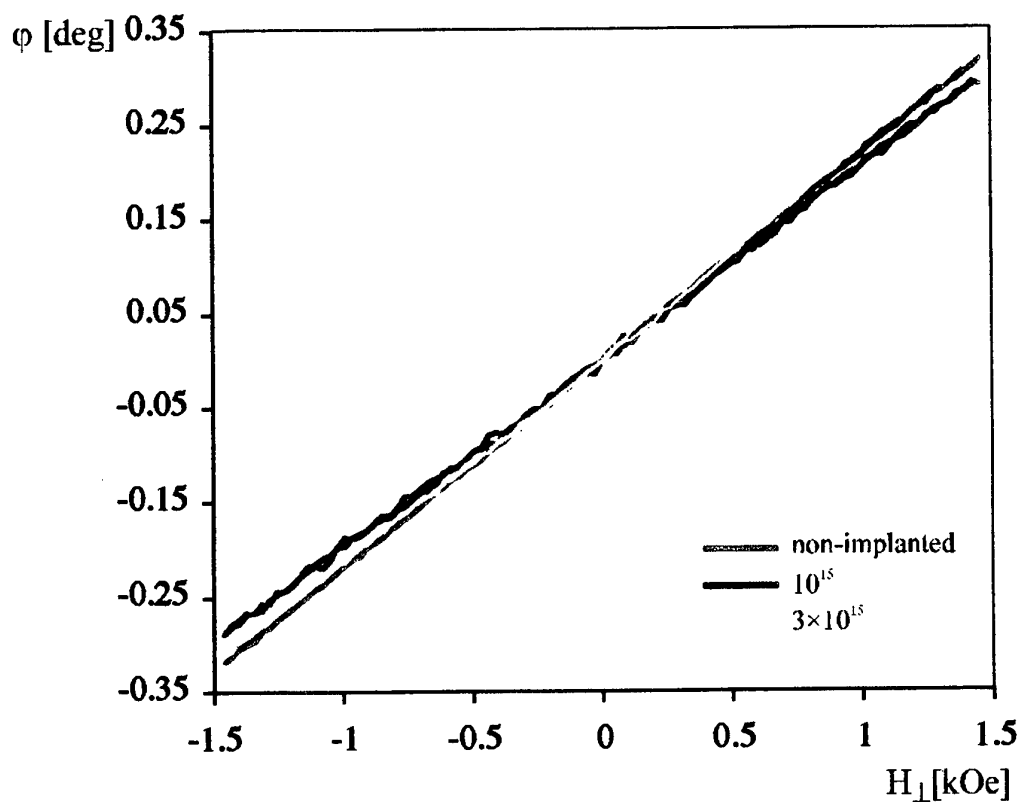


Figure 14 : Faraday rotation ϕ vs. magnetic field H_{\perp} measured for sample 2 at non-implanted area and D^{+} -implanted areas with energy 1.6 MeV and different doses.

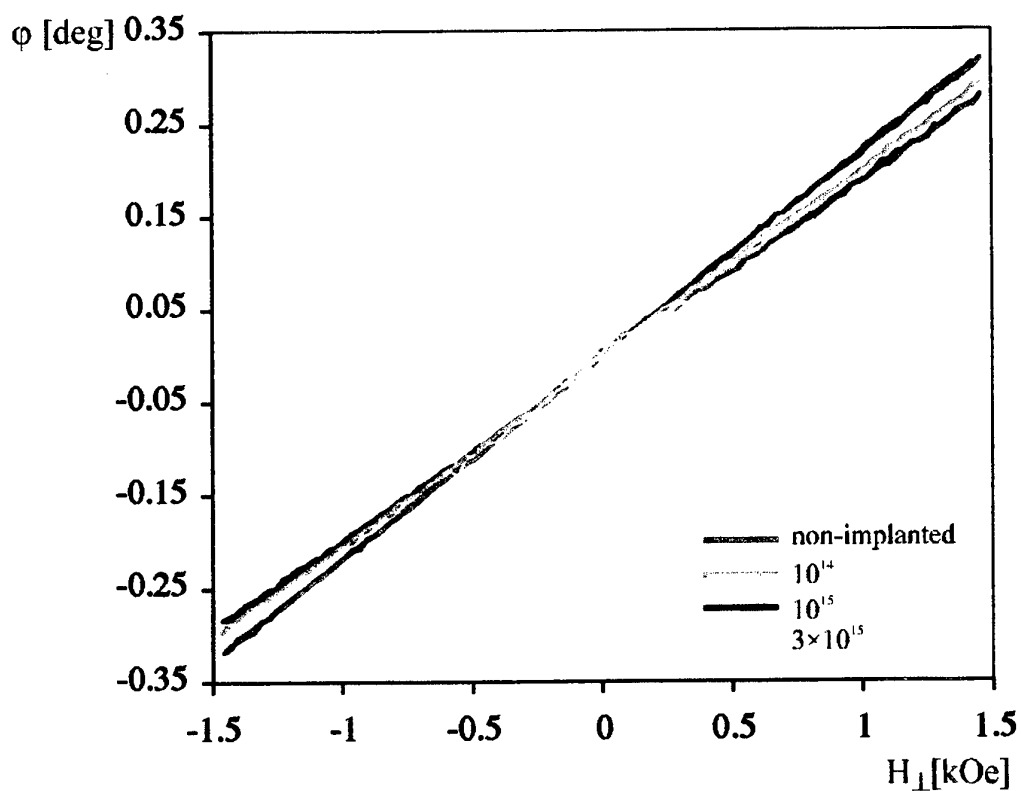


Figure 15 : Faraday rotation ϕ vs. magnetic field H_{\perp} measured for sample 2 at non-implanted area and D^{+} -implanted areas with energy 0.5 MeV and different doses.